# One-, Two-, and Three-channel Kondo effects for a model Ce<sup>3+</sup> Impurity in a Metal

Tae-Suk Kim and D. L. Cox

Department of Physics, Ohio State University, Columbus, Ohio 43210, USA
(August 16, 2018)

## Abstract

We present studies of a simple Anderson model Hamiltonian for Ce<sup>3+</sup> ions in cubic symmetry with three configurations  $(f^0, f^1, f^2)$ . Our Hamiltonian includes: (i) One-channel Anderson model; (ii) Two-channel Anderson model. Using the third order scaling analysis, we study stability of the non-Fermi liquid fixed point of the two-channel Kondo model for Ce<sup>3+</sup> ions in cubic symmetry against the one-channel Kondo interaction. Using the non-crossing approximation (NCA), we also report detailed studies of our simplified model of one-channel & two-channel Anderson model which exhibits competition between the Fermi-liquid fixed point of the one-channel Kondo model and the non-Fermi fixed point of the two-channel Kondo model. We provide the phase diagram in the model parameter space and study the thermodynamics and the transport properties of our simplified model Hamiltonian. Thermodynamics and transport coefficients show the distinct behaviors for different numbers of channels. We confirm in detail that the NCA is a valid numerical method for the overcompensated multichannel  $S_I=1/2$  Anderson models. Our model study might be relevant to the non-Fermi liquid alloy  $Ce_{1-x}La_xCu_{2.2}Si_2$ .

PACS Nos. 74.70.Vy, 74.65.+n, 74.70.Tx

#### I. INTRODUCTION

The Kondo effect [1] has been of great interest in condensed matter physics since its observation. The proposed model Hamiltonian, a magnetic  $S_I = 1/2$  local moment interacting with the conduction electron gas, looked very simple but was non-trivial due to many body nature of the problem. Ever since, many generalized models have been studied to extend our understanding and to relate to real materials. The simplest  $S_I=1/2$  orbitally nondegenerate Anderson model [2] and s-d exchange model are now well understood for a single impurity case using several techniques. The numerical renormalization group (NRG) [3] method was able to provide complete information about crossover from the high temperature fixed point to the low temperature fermi liquid fixed point for these models. Subsequently, the exact diagonalization of these models was realized by the Bethe Ansatz (BA) |4|, which also gives the exact solution for thermodynamics of these models. However, it has not proven possible to compute dynamical properties with the BA. Through non-crossing approximation (NCA) [5], dynamics as well as thermodynamics [6] have been extensively studied for the infinite on-site Coulomb interaction models. The Quantum monte Carlo method (QMC) [7] has also been applied to study statics and dynamics for the simple  $S_I=1/2$  models. Recently conformal field theory (CFT) [8,9] has been used to study all properties near the low temperature fixed points. However we are still far from a complete understanding for realistic models which, for example, include the strong spin-orbit coupling, the crystal electric field effects, and multiple (more than two) configurations. In this paper, we study a realistic extension of the conventional simple approach to the Kondo effect for  $Ce^{3+}$  ions, including the strong spin-orbit coupling, the crystal electric field effect, and multiple configurations in their simplest form.

Ever since Nozières and Blandin [10] introduced the multichannel Kondo model, its realization in real materials has been controversial. On the theoretical side, the multichannel Kondo models are well understood [8,11–13] irrespective of the experimental situations. When the degenerate channel number  $(N_{ch})$ , which is the number of the conduction electron "bands" coupled to the impurity site, is greater than  $2S_I$  (the impurity spin), the impurity magnetic moment is overscreened and the strong coupling fixed point (Fermi liquid) becomes unstable leading to a non-trivial fixed point (non-Fermi liquid behavior). In the underscreened and the completely screened cases,  $N_{\rm ch} \leq 2S_I$ , the strong coupling fixed point is stable resulting in a Fermi liquid ground state. The spin susceptibility  $\chi(T)$  and specific heat coefficient C(T)/T for the two-channel  $S_I = 1/2$  magnetic Kondo model are proportional to  $\log(T_K/T)$  at low temperatures [8,9,11–13], where  $T_K$  is the Kondo energy scale. The dynamic susceptibility shows Marginal Fermi liquid behavior [14]. The resistivity increases logarithmically and saturates to a constant with  $\rho(T) = \rho(0)$  [ $1 - a\sqrt{T/T_K}$ ] with decreasing temperature [8]. On the other hand, the one-channel  $S_I = 1/2$  Kondo model leads to the Fermi liquid ground state. In that case, magnetic susceptibility  $\chi(T)$  and specific heat coefficient C(T)/T saturate to constants of order  $1/T_K$  [3,4]. Resistivity increases logarithmically and saturates to a constant with  $\rho(T) = \rho(0)$  [ $1 - a(T/T_K)^2$ ] with decreasing temperature [15].

In this paper we study a model Hamiltonian for  $Ce^{3+}$  ions in cubic metals with three configurations  $(f^0, f^1, f^2)$ . The nominal ground configuration  $f^1$  can fluctuate to  $f^0$  and  $f^2$  configurations by hybridizing with the conduction electrons. A one-channel Anderson hybridization interaction is present between  $f^0$  and  $f^1$  configurations. A two-channel Anderson hybridization interaction is present between  $f^1$  and  $f^2$  configurations. We report detailed studies of our simplified Hamiltonian of one-channel & two-channel Anderson model using the NCA. This simple model is quite intriguing in that we can study the competition between the two different Kondo effects, that is, the Fermi liquid and the non-Fermi liquid fixed points. The distinct ground state physics for the different numbers of channels is classified using the zero temperature analysis of NCA integral equations and the third order scaling theory. We calculate the thermodynamics and the dynamics of this simple model and find that all the calculated physical quantities show the behavior appropriate for the accessible different channel numbers. The static magnetic susceptibility displays a scaling behavior agreeing with the exact Bethe ansatz results in the two- and three-channel cases.

NCA calculation of entropy and specific heat is also compared with the Bethe ansatz results. The resistivity shows the correct temperature dependence near zero temperature agreeing with the conformal field theory results in the two- and three-channel cases. The sign and the magnitude of the thermopower are dependent sensitively on the relevant channel numbers. The peak position in the dynamic magnetic susceptibility is almost linear in temperature in the overscreened cases. A short paper which presents some of these results will appear elsewhere [16].

Our study is motivated by a recent discovery of non-Fermi liquid system,  $Ce_xLa_{1-x}Cu_{2.2}Si_2$  (x = 0.1) [17]. We summarize the experimental findings of this alloy system. The logarithmic divergence in both the magnetic susceptibility  $\chi(T)$  and the specific heat linear coefficient  $\gamma(T)$  have been observed for  $\text{Ce}_x \text{La}_{1-x} \text{Cu}_{2.2} \text{Si}_2$  (x = 0.1). The two-channel  $S_I = 1/2$  magnetic Kondo physics [8,9,11–13] provides a theoretical framework to explain the thermodynamics of this system at low temperatures.  $\gamma(T)$  initially increases in the presence of the magnetic field, which qualitatively agrees with the two-channel Kondo effect coming from the lifting of residual entropy [13]. In the one-channel Kondo effect, the Sommerfeld coefficient decreases in the magnetic field due to the destruction of the Kondo effect. The Wilson ratio is estimated to be  $R\approx 2.7$  from the slopes of two curves  $(\chi(T))$ and  $\gamma(T)$ , which compares well with theoretical value 8/3 for the two-channel magnetic  $S_I = 1/2$  Kondo model [9]. The good agreement between the theoretical and the experimental Wilson ratios supports our crystalline electric field energy scheme described below. This system is pseudo-cubic (i.e., the crystal field scheme on the Ce<sup>3+</sup> site appears cubic). The best superconducting system with excess Cu shows almost isotropic magnetic susceptibility [18]. That the pseudo-cubic  $\Gamma_7$  magnetic doublet in  $f^1$  lies lowest is inferred from the neutron scattering experiments [19]. The thermopower for CeCu<sub>2</sub>Si<sub>2</sub> changes sign near 70 K and stays negative below with a large extremum (–20 to  $-30\mu\text{V/K}$ ) [18], suggesting the presence of strong hole resonance scattering. As we will show below, these thermopower results also support our interpretation of the two channel magnetic Kondo physics. Though other experiments (e.g., specific heat and magnetic susceptibility) support the interpretation of them in terms of the two-channel Kondo effect, a linear temperature dependence in the resistivity remains as a puzzle. The  $\sqrt{T}$  behavior in the resistivity is predicted from conformal field theory treatment of the two-channel Kondo models [8,9]. In Fig. 1, we present our numerical calculation of resistivity and the experimental results measured in the alloy system  $\text{Ce}_x\text{La}_{1-x}\text{Cu}_{2.2}\text{Si}_2$  (x=0.1) [17]. It can be seen that the data curves downwards at lower temperatures which may indicate a crossover to a new fixed point. From all these experimental findings, we believe that the alloy system  $\text{Ce}_x\text{La}_{1-x}\text{Cu}_{2.2}\text{Si}_2$  (x=0.1) is a strong candidate for two-channel  $S_I=1/2$  magnetic Kondo system.

In addition, the two-channel,  $S_I = 1/2$  Kondo effect may be realized in other materials: two-channel quadrupolar Kondo effect [20] in some U alloys and two-level systems [21] in metallic point contacts. U alloy systems include  $U_{0.2}Y_{0.8}Pd_3$  [22],  $U_xTh_{1-x}Ru_2Si_2$  [23],  $UCu_{3.5}Pd_{1.5}$  [24],  $U_{0.1}Th_{0.9}Ni_2Al_3$  [25],  $U_{0.1}Pr_{0.9}Ni_2Al_3$  [25],  $U_xSc_{1-x}Pd_3$  [26],  $U_{0.9}Th_{0.1}Be_{13}$  [27], and  $U_xTh_{1-x}Pd_2Al_3$  [29]. All the above systems show a logarithmic divergence at low temperature in the linear specific heat coefficient and a square root saturation in the static magnetic susceptibility.  $U_xTh_{1-x}Ru_2Si_2$  [23] is an exception showing a logarithmically divergent magnetic susceptibility. The two channel quadrupolar Kondo physics has been invoked to explain non-Fermi liquid behavior in thermodynamic and transport properties of  $U_xY_{1-x}Pd_3$  for x=0.2 [22] and other U alloy systems. Recently, the resistivity in a metallic constriction was observed to obey  $\sqrt{T}$  behavior and was interpreted as due to two-channel Kondo scattering from atomic two-level tunneling systems [30,31].

Our paper is organized as follows. In section II, we introduce our simple model Hamiltonian and analyze this model using the third order scaling equation. We briefly introduce the NCA in section III. Zero temperature analysis of NCA integral equations follows in section IV. In section V, we present the detailed numerical analysis of our simple model Hamiltonian. We conclude in the section VI.

#### II. MODEL HAMILTONIAN

The single impurity Anderson model [2] has been very successful [6] in describing Kondo systems (meaning magnetic transition metal elements embedded in normal metals, and dilute rare earth or actinide alloys). The thermodynamics is rather well explained by the single impurity properties for even highly concentrated Ce alloys [6,32]. Coherence effects, arising from the lattice of Anderson or Kondo ions at low temperatures, do not play such an important role in thermodynamics. Transport properties also are well explained by the single impurity model except for the low temperature regime where a coherence effect prevails due to the coherent Bloch state formation leading to vanishing resistivity at zero temperature (the residual resistivity is larger than the room temperature one in the dilute impurity limit). This one-channel Anderson model can explain the complete screening of the magnetic moment at the local moment sites leading to the local Fermi liquid ground state discussed in the introduction.

The two-channel orbital Kondo model (quadrupolar or two-level system) keeps the channel symmetry guaranteed by time reversal symmetry, but can suffer from the ground state degeneracy lifting due to the Jahn-Teller effect. In general, the orbital Kondo model has the exchange anisotropy. It has been shown that the exchange anisotropy is irrelevant for the two-channel  $S_I = 1/2$  Kondo models [33]. As will be shown in other publication [34], the two-channel magnetic Kondo model for  $Ce^{3+}$  is vulnerable to the channel asymmetry due to its orbital nature in the channel degrees of freedom [10]. However, the channel-mixing Kondo interaction can save the two-channel physics [34].

The conventional theory of  $Ce^{3+}$  impurities assumes the infinite on-site Coulomb interaction, which removes the  $f^2$  configuration from consideration [6], and as a result has no chance to get the two-channel Kondo effect which we shall explain below. When we relax our assumption about the strong on-site Coulomb interaction and we include the detailed atomic energy structure, we can develop a variety of model Hamiltonians [34].

In our simple model, we assume the magnetic  $f^1$  J = 5/2  $\Gamma_7$  CEF doublet lies lowest in

the  $f^1$  configuration, and we keep the two excited states – a singlet  $f^0$  and the nonmagnetic  $f^2$   $\Gamma_3$  CEF doublet. We find the one-channel Anderson model in mixing between  $f^0$  and  $f^1$  configurations and the two-channel Anderson model in mixing between  $f^1$  and  $f^2$  configurations [35]. Other interesting Kondo interactions [34] arise when the excited triplets in the  $f^2$  configuration are included. According to the group theory analysis, the hybridization is mediated only by the cubic  $\Gamma_8$  conduction electrons between  $f^1$  and  $f^2$  ( $\Gamma_3 \otimes \Gamma_7 = \Gamma_8$ ), and by  $\Gamma_7$  between  $f^0$  and  $f^1$  for the mixing potential allowed in the cubic crystal. CEF states are schematically drawn in the Fig. 2 for this simple model. To see the essential physics, we restrict our attention to the simple case of isotropic hybridization and a free conduction band with Lorentzian/Gaussian density of states (DOS). In this simple case, two components of conduction partial wave  $j_c = 5/2, 7/2$  can mix with the atomic orbitals. For the moment, we will consider only one angular momentum component, say,  $j_c = 5/2$  of the conduction band for our model study. We shall examine the effects of relaxing this in the other paper [34]. Our model Hamiltonian is

$$H = H_{\rm cb} + H_{\rm at} + H_1,\tag{1}$$

$$H_{\rm cb} = \sum_{\epsilon\alpha} \epsilon c_{\epsilon\Gamma_7\alpha}^{\dagger} c_{\epsilon\Gamma_7\alpha} + \sum_{\epsilon n\alpha} \epsilon c_{\epsilon\Gamma_8n\alpha}^{\dagger} c_{\epsilon\Gamma_8n\alpha}, \tag{2}$$

$$H_{\rm at} = \epsilon_0 |f^0\rangle \langle f^0| + \epsilon_1 \sum_{\alpha} |f^1 \Gamma_7 \alpha\rangle \langle f^1 \Gamma_7 \alpha| + \epsilon_2 \sum_{n} |f^2 \Gamma_3 n\rangle \langle f^2 \Gamma_3 n|, \tag{3}$$

$$H_{1} = V_{01} \sum_{\epsilon \alpha} c_{\epsilon \Gamma_{7} \alpha}^{\dagger} |f^{0}\rangle \langle f^{1} \Gamma_{7} \alpha| + h.c.$$

$$+ V_{12} \sum_{\epsilon n \alpha} (-1)^{\alpha + 1/2} c_{\epsilon \Gamma_{8} n \alpha}^{\dagger} |f^{1} \Gamma_{7} \bar{\alpha}\rangle \langle f^{2} \Gamma_{3} n| + h.c.$$

$$(4)$$

 $c_{\epsilon\Gamma_7\alpha}(c_{\epsilon\Gamma_7\alpha}^{\dagger})$  and  $c_{\epsilon\Gamma_8n\alpha}(c_{\epsilon\Gamma_8n\alpha}^{\dagger})$  are the annihilation (creation) operators for conduction electrons of  $\Gamma_7$  and  $\Gamma_8$ , respectively.  $\alpha=\uparrow,\downarrow$  denotes the time reversal pair for the irreducible  $\Gamma_7$  representation, and  $n=\pm$  is the quadrupolar index for  $\Gamma_3$  and here acting as the channel indices. The conduction electrons are assumed to be described by the uncorrelated Lorentzian/Gaussian density of states with bandwidth D=3 eV.  $\epsilon_{0,1,2}$  are the configuration energies for the empty ( $\epsilon_0=0$ ), single, and double occupancies, respectively. We lumped all Clebsch-Gordon coefficients into the hybridization constants,  $V_{01}$  and  $V_{12}$ , except for the phase dependence on the cubic degeneracy indices. The phase dependence on the Kramers

doublet index comes from time reversal symmetry. We will consider these two hybridization constants to be independent of each other to probe the competition between the one-channel and the two-channel Kondo physics.

When the real charge fluctuations are removed from the model system in the Kondo limit, we have to construct the tensor operators representing each CEF states for the  $f^1$ configuration and the projected conduction electron CEF states. In this paper, the relevant tensor operators are for  $\Gamma_{7,8}$  CEF states. We can show using the character table [36] that

$$\Gamma_7 \otimes \Gamma_7 = \Gamma_1 \oplus \Gamma_4,\tag{5}$$

$$\Gamma_8 \otimes \Gamma_8 = \Gamma_1 \oplus \Gamma_2 \oplus \Gamma_3 \oplus 2\Gamma_4 \oplus 2\Gamma_5. \tag{6}$$

In the direct product, the first CEF states are written as ket, and the second as bra. The  $\Gamma_7$  tensor operator (2 × 2 tensor) is a direct sum of charge operator ( $\Gamma_1$ ) and spin operator ( $\Gamma_4$ ). Indeed, the Schrieffer-Wolff transformation leads to two interaction terms: the spin exchange interaction and the pure potential scattering term. The relevant terms of  $\Gamma_8$  tensor operators are  $2\Gamma_4$  in our model. In the conduction electron  $\Gamma_8$  tensor space, one of the two  $\Gamma_4$ 's gives rise to the ordinary  $S_c = 1/2$  spin operators with two degenerate orbital channels and the other to the  $S_c = 3/2$  spin operator with one channel [34].

Hence, there are three distinct channel labels for conduction electron partial wave states about the Ce impurity in this simple model. One channel is just the  $\Gamma_7$  doublet. The other two are the  $\Gamma_3\pm$  "orbital" states of the  $\Gamma_8$  quartet. Each  $\Gamma_3\pm$  orbital has a  $\Gamma_7$  "spin" doublet (recall  $\Gamma_8 = \Gamma_7 \otimes \Gamma_3$ .) As shown in Fig. 3 for J = 5/2 conduction partial waves, the + orbital is "stretched" along the quantized axis (one of the three principal cubic axes, taken to be  $\hat{z}$  here for definiteness.) The "-" orbital is "squashed" in the xy plane. We note that the simplest example of  $\Gamma_8$  partial wave quartet is, for zero spin-orbit coupling, d-wave states with  $+ \to 3z^2 - r^2$  and  $- \to x^2 - y^2$ . The "spin" index is then real spin of the electrons.

In the Kondo limit with the stable  $f^1$  configuration, we may remove the  $f^0 - f^1$ ,  $f^1 - f^2$  charge fluctuations from the Hamiltonian of Eq. (4) using the Schrieffer-Wolff transformation [37] to find the effective Hamiltonian.

$$\tilde{H}_1 = J_1 \vec{S}_{c\Gamma_7}(0) \cdot \vec{S}_{\Gamma_7} + J_2 \sum_{n=+} \vec{S}_{c\Gamma_8 n}(0) \cdot \vec{S}_{\Gamma_7}$$
(7)

$$J_1 = \frac{2|V_{01}|^2}{-\epsilon_1}, \quad J_2 = \frac{2|V_{12}|^2}{\epsilon_2 - \epsilon_1},$$
 (8)

$$\vec{S}_{\Gamma_7} = \frac{1}{2} \sum_{\alpha\beta} |f^1; \Gamma_7 \alpha > \vec{\sigma}_{\alpha\beta} < f^1; \Gamma_7 \beta|. \tag{9}$$

 $\vec{S}_{\Gamma_7}$  is the  $f^1$  pseudo spin.  $\vec{S}_{c\Gamma_7}(0)$  and  $\vec{S}_{c\Gamma_8\pm}(0)$  are the conduction electron pseudo spin densities at the impurity site of symmetry  $\Gamma_7$  and  $\Gamma_8$ , respectively. When the  $f^1$  configuration is stable, its pseudo spin is coupled to the conduction band in a one-channel via  $f^0$  configuration, and in a two-channel via  $f^2$  configuration. Their couplings are both antiferromagnetic. The unique feature of our Hamiltonian is that it can generate the one-, two-, and three-channel ground states depending on the model parameters. The competition between the Fermi liquid fixed point and the non-Fermi liquid fixed point can thus be investigated using this model Hamiltonian.

We first analyze our simple model Hamiltonian using the third order scaling argument, i.e., the perturbative renormalization group (RG) [10,38]. At temperature T, only the conduction electrons (thermally excited) inside the band of order T with respect to the Fermi level play an important role in determining physical properties. Thus we can integrate out the band edge states (virtually excited states) to find the effective Hamiltonian. Though the following analysis is restricted to  $\omega \ll D$  (the conduction band width) and the perturbative regime (weak coupling limit), we can derive qualitative results out of this. For quantitative results, a full numerical renormalization group (NRG) study is required.

It can be deduced from the scaling theory that the low temperature and the low energy physics is dominated by the one-channel or the two-channel Kondo effects depending on their relative magnitude of the antiferromagnetic couplings. We introduce an exchange coupling matrix in the channel space which is convenient for the derivation of the scaling equations. We can thus rewrite the one-channel and two-channel Kondo model in the following form [34].

$$\tilde{H}_1 = \mathbf{J} \otimes \vec{S}_c(0) \cdot \vec{S}_I, \tag{10}$$

$$\mathbf{J} = \begin{pmatrix} J_1 & 0 & 0 \\ 0 & J_2 & 0 \\ 0 & 0 & J_2 \end{pmatrix}. \tag{11}$$

Here  $\vec{S}_c$  and  $\vec{S}_I$  are S=1/2 operators. The scaling equations of our simple model Hamiltonian up to the third order diagrams of Fig. 4 are

$$\frac{\partial \mathbf{g}}{\partial x} = \mathbf{g}^2 - \frac{1}{2} \mathbf{g} \operatorname{Tr}[\mathbf{g}^2], \tag{12}$$

$$\mathbf{g} = N(0)\mathbf{J}.\tag{13}$$

The scaling equations in components are

$$\frac{\partial g_1}{\partial x} = g_1^2 - \frac{1}{2} g_1 \left[ g_1^2 + 2g_2^2 \right], \quad g_1 = N(0)J_1 > 0, \tag{14}$$

$$\frac{\partial g_2}{\partial x} = g_2^2 - \frac{1}{2} g_2 \left[ g_1^2 + 2g_2^2 \right], \quad g_2 = N(0)J_2 > 0. \tag{15}$$

Here  $x = \log(D/T)$ . We can identify three fixed points related to one-, two-, and three-channel Kondo physics. The one-channel, strong coupling fixed point  $(g_1^*, g_2^*) = (\infty, 0)$  is stable leading to the Fermi liquid ground state [38]. The three-channel fixed point (2/3, 2/3) is stable along the line  $g_1 = g_2$  in the  $g_1 - g_2$  plane, but unstable for any small perturbation from  $g_1 = g_2$ . Finally, the two-channel fixed point (0, 1) is stable leading to the logarithmically divergent thermodynamic properties at zero temperature. From the scaling analysis, we can infer the ground state physics: one-channel for  $J_1 > J_2$ ; two-channel for  $J_1 < J_2$ ; and three-channel for  $J_1 = J_2$ . As will be shown in section IV, the zero temperature analysis of the NCA equations leads to the same conclusion.

We now discuss the neglected other 8  $\Gamma_3$  irreps in the  $f^2$  configuration [34]. The 9  $\Gamma_3$  CEF states all contribute to the enhancement of the two-channel exchange coupling between  $f^1\Gamma_7$  spin and the  $\Gamma_8$  conduction electron spins.

$$H_1 = \sum_{\epsilon} \sum_{in\alpha} (-1)^{\alpha+1/2} V_{12}^i \ c_{\epsilon \Gamma_8 n\alpha}^{\dagger} \ |f^1 \Gamma_7 \bar{\alpha} \rangle \langle f^2 \Gamma_3^i n| + h.c.$$
 (16)

The NCA can treat this problem with the extension that now the  $f^2$   $\Gamma_3$  Green's function becomes an  $9 \times 9$  matrix. See the Appendix for more details. The Schrieffer-Wolff transformation leads to

$$\tilde{H}_1 = J \sum_{n=+} \vec{S}_{c\Gamma_8 n} \cdot \vec{S}_{\Gamma_7}, \tag{17}$$

$$J = \sum_{i=1}^{11} \frac{2|V_{12}^i|^2}{\epsilon_2^i - \epsilon_1}.$$
 (18)

Here  $\epsilon_2^i$  is the energy level for the *i*-th  $f^2\Gamma_3$  state. Hence multiple  $\Gamma_3$  states in the  $f^2$  configuration lead to the enhancement of the two-channel exchange coupling.

Particle-hole asymmetry in the conduction band density of states (DOS) is also important in determining the ground state weights of the one-channel  $(f^0 - f^1)$  and the two-channel  $(f^1 - f^2)$  contributions. In the scaling approach, the particle-hole asymmetry is completely neglected. However the NCA can take into account this particle-hole asymmetry. The occupied conduction electron states (hole) contribute to the  $f^0$  self energy (see the section III), while the unoccupied states (particle) to the  $f^2$  self energy. Hence the more weight in the particle side can enhance the effective hybridization strength between  $f^1$  and  $f^2$  configurations. The particle-dominant conduction band DOS will lead to the enhancement of the two-channel exchange coupling.

### III. NON-CROSSING APPROXIMATION (NCA).

We now apply the non-crossing approximation (NCA) [5] to study our simple model system – one-channel & two-channel Anderson model. Though this model is highly simplified compared with the full model [34], we can simulate the full model using this simple model Hamiltonian to study the different physics for varying channel number.

In the NCA, our starting basis is the conduction band plus the atomic Hamiltonian projected to the atomic electron Fock space and treat the hybridization between the conduction band and the atomic orbital as a perturbation. The strength of this approach is that the strong on-site Coulomb interaction for atomic electrons is treated accurately at the outset. Pseudo particle Green's functions are introduced for each atomic electron occupation state which is neither fermionic nor bosonic. The price we pay is that we cannot apply the conventional Feynmann diagram techniques to this strongly correlated problems. Thus special

Green's function technique was developed by many investigators [5,6,39–42]. This approach may be justified by expansion in 1/N which reorders the diagrams by treating  $NV^2$  as  $\mathcal{O}(1)$ . Here N is the nominal atomic ground state degeneracy and V is the hybridization strength between the conduction band and the atomic orbitals. In the NCA, pseudo particle self energy diagrams include only the leading order skeleton (non-crossing) diagrams and they are solved self-consistently. For the one-channel models, this theory includes all the diagrams up to  $\mathcal{O}(1/N)$  order and a subset of higher order diagrams up to the infinite order. Though vertex corrections, which is  $\mathcal{O}(1/N^2)$ , are not included, this approach is a conserving approximation [40]. For the overscreened multi-channel Anderson models, it has been shown [14] that the 1/N approach becomes exact in the limit  $M, N \to \infty$  with fixed M/N ratio (M) is the number of channels).

When we study the most general three-configuration model, the same symmetry conduction electron can be involved in the two mixing processes, e.g.,  $f^0 - f^1$  and  $f^1 - f^2$  for  $Ce^{3+}$  atoms. Generally, a specific vertex correction is required to get the right Kondo energy scales in this case. Recently, vertex corrections were included in the study of the finite U spin 1/2 Anderson model [43]. A simplifying feature of our model Hamiltonian is that the leading vertex correction vanishes, since two different symmetry conduction electrons are involved in the hybridizations  $f^0 - f^1$  ( $\Gamma_7$ ) and  $f^1 - f^2$  ( $\Gamma_8$ ). This feature greatly simplifies the numerical work and formalism.

From the leading order skeleton diagrams of Fig. 5, we find the self-consistent integral equations:

$$\Sigma_0(z) = \frac{\Gamma_{01}}{\pi} \sum_{\alpha} \int d\epsilon \ \tilde{N}(\epsilon) f(\epsilon) G_1(z + \epsilon), \tag{19}$$

$$\Sigma_{1}(z) = \frac{\Gamma_{01}}{\pi} \int d\epsilon \ \tilde{N}(\epsilon) f(-\epsilon) G_{0}(z - \epsilon) + \frac{\Gamma_{12}}{\pi} \sum_{n} \int d\epsilon \ \tilde{N}(\epsilon) f(\epsilon) G_{2}(z + \epsilon),$$
(20)

$$\Sigma_2(z) = \frac{\Gamma_{12}}{\pi} \sum_{\alpha} \int d\epsilon \ \tilde{N}(\epsilon) f(-\epsilon) G_1(z - \epsilon), \tag{21}$$

$$G_N(z) = \frac{1}{z - \epsilon_N - \Sigma_N(z)}, \quad \Gamma_{ij} \equiv \pi N(0) |V_{ij}|^2.$$
 (22)

Here  $\tilde{N}(\epsilon)$  is the normalized conduction band DOS at the fermi level such that  $\tilde{N}(0) = 1$ .  $\Sigma_{0,1,2}(z)$  and  $G_{0,1,2}(z)$  are the self energy equations and Green's functions for  $f^0$ ,  $f^1\Gamma_7$ , and  $f^2\Gamma_3$  atomic states, respectively.  $f(\epsilon)$  is the Fermi-Dirac distribution function.  $\Gamma_{ij}$  is the hybridization strength characterizing the width of the renormalized atomic electron spectral function peak. One of the strong points of the NCA approach is that we can easily study any form of the conduction band DOS, as opposed to other approaches, e.g., Bethe ansatz or conformal field theory, to Anderson/Kondo models. As a concrete example, we will use the structureless Lorentzian/Gaussian DOS to see the many body physics. We solved these coupled integral equations numerically to study the thermodynamics and the dynamics of the model Hamiltonian.

Pseudo particle Green's functions are not directly measurable. All the physically measurable quantities are given by the convolution of the pseudo particle Green's functions. Now it is convenient to introduce the spectral function  $(A_N(\omega))$  for each pseudo particle Green's function and its negative frequency spectral function  $(a_N(\omega))$ .

$$A_N(\omega) \equiv -\frac{1}{\pi} \operatorname{Im} \frac{1}{\omega - \epsilon_N - \Sigma_N(\omega)}, \tag{23}$$

$$a_N(\omega) \equiv e^{-\beta\omega} A_N(\omega).$$
 (24)

Since  $a_N(\omega)$  always appears in combination with the impurity partition function  $Z_f$ , there is arbitraryness in overall factor in its definition. The above NCA integral equations do not have  $a_N(\omega)$  in them. Whenever we calculate any measurable physical quantities, the spectral functions appear with the Boltzman thermal factor divided by the impurity partition function. In the numerical work, we calculate  $a_N(\omega)$ 's self-consistently. Roughly speaking,  $a_N(\omega)$ 's are occupancy distribution function weighted by the thermal factor.

The impurity partition function for our simple model is defined by

$$Z_{\rm f} \equiv \int d\omega \ \left[ a_0(\omega) + 2a_1(\omega) + 2a_2(\omega) \right]. \tag{25}$$

This partition function includes the many body effect of the interaction between impurity and the conduction band and is exact in its form. The approximation comes in when we choose the approximate Green's functions for the atomic states.

In our simple model, only two symmetry electrons are present:  $\Gamma_7$  and  $\Gamma_8$ . Their spectral functions (measurable) are defined as a convolution of two neighboring configurations' spectral functions. It can be shown that these two interconfiguration atomic spectral functions are given by

$$\rho_{\Gamma_7}(\omega) = \frac{1 + e^{-\beta \omega}}{Z_f} \int d\zeta \ a_0(\zeta) \ A_1(\zeta + \omega) = \rho_{01}(\omega), \tag{26}$$

$$\rho_{\Gamma_8}(\omega) = \frac{1 + e^{-\beta \omega}}{Z_f} \int d\zeta \ a_1(\zeta) \ A_2(\zeta + \omega) = \rho_{12}(\omega)$$
 (27)

in this conserving approximation [40]. From now on, we will use the notations  $\rho_{01}$ ,  $\rho_{12}$  in favor of  $\rho_{\Gamma_7}$ ,  $\rho_{\Gamma_8}$ . This approximation does not include any vertex correction.

From the leading bubble diagram [6], the static magnetic susceptibility per Ce<sup>3+</sup> impurity is

$$\chi(T) = \frac{1}{3} \mu_{\text{eff}}^2 \tilde{\chi}_f(T), \quad \mu_{\text{eff}}^2 = \frac{75}{49} \mu_{\text{B}}^2,$$
(28)

$$\tilde{\chi}(T) = -\frac{4}{Z_{\rm f}} \int d\zeta \ a_1(\zeta, T) \ \text{Re}G_1(\zeta, T). \tag{29}$$

Here  $\mu_{\rm B}$  is Bohr magneton. The reduced dynamic magnetic susceptibility is

$$\tilde{\chi}''(\omega, T) = \frac{1 - e^{-\beta \omega}}{Z_{\rm f}} \int d\zeta \ a_1(\zeta, T) \ A_1(\zeta + \omega, T). \tag{30}$$

We are going to calculate these physical quantities and transport coefficients.

#### IV. ZERO TEMPERATURE ANALYSIS.

Zero temperature analysis [14,44] of the NCA integral equations leads to a qualitative understanding of our model system. Recently, conformal field theory approach [8] calculated the scaling dimensions exactly for the multi-channel Kondo exchange models with any size of impurity spin. In Ref. [14], the evaluation of the scaling dimensions is extended to the multichannel Anderson/Coqblin-Schrieffer models using the functional integral formulation. Both models become congruent when the impurity spin is  $S_I = 1/2$ .

The main results of the zero temperature analysis of the NCA integral equations are: (1) We can find the criterion which predicts whether the ground state is that of the 1, 2, or 3 channel model. (2) The Kondo energy scale  $(T_0)$  can be estimated analytically for the case  $\Gamma_{01} = \Gamma_{12}$ .  $T_0$  in the one- and two-channel model parameter regimes is shown to vanish as the  $f^2$   $\Gamma_3$  energy level approaches that of the  $f^0$  configuration. (3) We obtain the correct scaling dimensions for the overcompensated cases which agree with the conformal field theory results [9]. (4) The crossover physics between the parameter regimes for different numbers of channels can be identified.

The self consistent NCA integral equations can be transformed into the differential equations for the flat conduction band in the wide band limit:  $D \gg |\epsilon_{1,2}|$ . We analyze the zero temperature NCA equations in the asymptotic limit  $|\omega - E_0| \ll T_0$ .  $E_0$  is the threshold energy below which the pseudo particle Green's functions become purely real. We introduce the inverse Green's functions and transform the self energy equations at zero temperature into the coupled non-linear differential equations. [44]

$$g_0(\omega) \equiv -1/G_0(\omega); \quad g_1(\omega) \equiv -1/G_1(\omega); \quad g_2(\omega) \equiv -1/G_2(\omega),$$
 (31)

$$\frac{d}{d\omega}g_0(\omega) = -1 - \frac{2\Gamma_{01}}{\pi} \frac{1}{g_1(\omega)}; \quad g_0(-D) = D,$$
(32)

$$\frac{d}{d\omega}g_1(\omega) = -1 - \frac{\Gamma_{01}}{\pi} \frac{1}{g_0(\omega)} - \frac{2\Gamma_{12}}{\pi} \frac{1}{g_2(\omega)}; \quad g_1(-D) = D + \epsilon_1, \tag{33}$$

$$\frac{d}{d\omega}g_2(\omega) = -1 - \frac{2\Gamma_{12}}{\pi} \frac{1}{g_1(\omega)}; \quad g_2(-D) = D + \epsilon_2.$$
 (34)

Then  $g_0$  and  $g_2$  can be shown to be related by

$$\frac{g_2}{\Gamma_{12}} = \frac{g_0}{\Gamma_{01}} + \left[\frac{1}{\Gamma_{01}} - \frac{1}{\Gamma_{12}}\right] (\omega - E_0) + \gamma_c, \tag{35}$$

$$\gamma_c = \frac{\epsilon_2 - E_0}{\Gamma_{12}} + \frac{E_0}{\Gamma_{01}}.\tag{36}$$

In the zero temperature analysis, it is more convenient to define the "negative frequency" spectral functions by  $a_i(\omega) \equiv e^{-\beta\omega} A_i(\omega)/Z_f$ . These spectral functions vanish above the threshold energy  $E_0$  and satisfy

$$\frac{d}{d\omega}[a_0(\omega)|g_0(\omega)|^2] = -\frac{2\Gamma_{01}}{\pi}a_1(\omega), \tag{37}$$

$$\frac{d}{d\omega}\left[a_1(\omega)|g_1(\omega)|^2\right] = -\frac{\Gamma_{01}}{\pi}a_0(\omega) - \frac{2\Gamma_{12}}{\pi}a_2(\omega),\tag{38}$$

$$\frac{d}{d\omega}[a_2(\omega)|g_2(\omega)|^2] = -\frac{2\Gamma_{12}}{\pi} a_1(\omega). \tag{39}$$

It can be shown from the above relations that

$$\frac{d}{d\omega} \left[ a_0(\omega)g_0(\omega) + 2a_1(\omega)g_1(\omega) + 2a_2(\omega)g_2(\omega) \right] = a_0(\omega) + 2a_1(\omega) + 2a_2(\omega). \tag{40}$$

By integrating this equation from  $\omega = -\infty$  to  $\omega = E_0$ , we find the additional relation,

$$[a_0(\omega)g_0(\omega) + 2a_1(\omega)g_1(\omega) + 2a_2(\omega)g_2(\omega)]_{\omega = E_0} = 1.$$
(41)

This identity will be useful in finding the asymptotic behavior of the "negative frequency" spectral functions. As a corollary, we have another identity in the asymptotic limit,

$$\frac{a_0(\omega)|g_0(\omega)|^2}{\Gamma_{01}} = \frac{a_2(\omega)|g_2(\omega)|^2}{\Gamma_{12}}.$$
(42)

This relation can be proved by using the boundary condition at  $\omega = E_0$ . We calculate the physical atomic spectral functions and the dynamic magnetic susceptibility defined in section IV.

$$\rho_{01}(\omega) = \int d\epsilon \left[ a_0(\epsilon) A_1(\epsilon + \omega) + A_0(\epsilon) a_1(\epsilon + \omega) \right], \tag{43}$$

$$\rho_{12}(\omega) = \int d\epsilon \ \left[ a_1(\epsilon) A_2(\epsilon + \omega) + A_1(\epsilon) a_2(\epsilon + \omega) \right], \tag{44}$$

$$\tilde{\chi}''(\omega) = \int d\epsilon \ [a_1(\epsilon)A_1(\epsilon + \omega) - A_1(\epsilon)a_1(\epsilon + \omega)]. \tag{45}$$

From the  $\omega$  dependence of the spectral functions near  $\omega = 0$ , we can infer the finite temperature dependence of transport coefficients as will be discussed below.

We now discuss the phase diagram in the model parameter space using the zero temperature analysis.  $\gamma_c$  decides the low energy and the low temperature behaviors of our model Hamiltonian.  $\gamma_c$  measures the relative magnitude of the antiferromagnetic coupling strengths when the charge fluctuation is removed in the model Hamiltonian. Noting that  $E_0 \approx \epsilon_1 + \mathcal{O}(V_{01}^2, V_{12}^2)$ , we find

$$\gamma_c \approx \frac{2}{\pi N(0)} \left[ \frac{1}{J_2} - \frac{1}{J_1} \right] \tag{46}$$

which illustrates the correspondence to the scaling analysis. If  $\gamma_c$  is greater than zero, the singular behavior shows up in the  $f^0$  Green's function, and not in the  $f^2$  Green's function. Hence the system will be dominated by the  $f^0$  and  $f^1$  sector leading to the one-channel Kondo effect. When  $\gamma_c$  is less than zero, the singular behavior shows up in the  $f^2$  Green's function, and not in the  $f^0$  Green's function. In this case  $f^1$  and  $f^2$  sector (the two-channel Kondo physics) determines the low temperature behavior of the system. When  $\gamma_c = 0$ ,  $f^0$  and  $f^2$  become equivalent asymptotically ( $|\omega - E_0| \ll T_0$ ). Both Green's functions develop the singular behaviors at the ground state energy. In this model parameter space, the three-channel Kondo model is realized.

The characteristic Kondo energy scale  $T_0$  is found from an integration constant which connects the low and high energy states. We can obtain the integration constant for the case  $\Gamma_{12} = \Gamma_{01} (= \Gamma)$ . We will analyze this case in detail and indicate subsequently how to extend the zero temperature analysis to the general hybridization strength.

# **A.** The symmetric hybridization limit: $\Gamma_{12} = \Gamma_{01} (= \Gamma)$ .

When we take a symmetric hybridization limit  $\Gamma_{12} = \Gamma_{01} (= \Gamma)$ , the equations are simplified.

$$\gamma_c = \frac{\epsilon_2}{\Gamma},\tag{47}$$

$$g_2 = g_0 + \epsilon_2, \tag{48}$$

$$a_0 g_0^2 = a_2 g_2^2. (49)$$

The last two relations hold true in the asymptotic limit,  $|\omega - E_0| \ll T_0$ . The different ground states then are determined solely by the sign of the  $f^2$  configuration energy relative to the  $f^0$  configuration energy. Removing the variable  $\omega$ , we can find the differential equations between the inverse Green's functions. Integrating from their values at  $\omega = -D$  to those at  $\omega$ , we find the integration constant

$$\exp\left[\frac{\pi}{2\Gamma}\left[g_0 - g_1 + \epsilon_1\right]\right] = \left[\frac{g_1}{D}\right] \left[\frac{g_0}{D}\right]^{-1/2} \left[\frac{g_0 + \epsilon_2}{D}\right]^{-1} \tag{50}$$

in the wide conduction band limit,  $D >> |\epsilon_{1,2}|$ . We identify three cases for evaluating  $T_0$ . (1) One-channel case:  $\gamma_c > 0$  or  $\epsilon_2 > 0$ .  $f^0$  Green's function develops a singular behavior at the threshold energy, while  $f^2$  Green's function does not. Thus the ground state physics is dominated by the sector  $f^0 - f^1$  leading to the one-channel Kondo effect. The integration constant and the Kondo temperature are

$$\frac{g_1}{T_0} = \left[\frac{g_0}{\Delta}\right]^{1/2} \left[1 + \frac{g_0}{\epsilon_2}\right] \exp\left[\frac{\pi(g_0 - g_1)}{2\Gamma}\right],\tag{51}$$

$$T_0 = D \left[\frac{\epsilon_2}{D}\right] \left[\frac{\Gamma}{\pi D}\right]^{1/2} \exp\left[\frac{\pi \epsilon_1}{2\Gamma}\right].$$
 (52)

Here  $\Delta \equiv \Gamma/\pi$ . We can find the asymptotic behavior of the Green's functions for each atomic state.

$$\frac{g_0(\omega)}{\Delta} \approx \tilde{\Omega}^{\alpha_0},\tag{53}$$

$$\frac{g_1(\omega)}{T_0} \approx \tilde{\Omega}^{\alpha_1},\tag{54}$$

$$g_2(\omega) = g_0(\omega) + \epsilon_2, \tag{55}$$

$$\tilde{\Omega} = 3 \frac{E_0 - \omega}{T_0},\tag{56}$$

$$\alpha_0 = \frac{2}{3}; \quad \alpha_1 = \frac{1}{3}.$$
 (57)

Though the scaling dimension is not correct, the estimated Kondo temperature is correct within order unity and  $\chi(0) \sim 1/T_0$ . An interesting observation is that Kondo temperature vanishes as  $\epsilon_2$  tends to zero, i.e., the three-channel parameter regime (see the discussion below).

The detailed derivation of the asymptotic behavior is not included since NCA does not produce the Fermi liquid ground state in the one-channel model. We just give a brief summary of the zero temperature analysis which is relevant to our study.  $A_2(\omega)$  vanishes as  $\tilde{\Omega}^{2/3}$  at the threshold energy, while  $A_0$  ( $A_1$ ) is singular as  $\tilde{\Omega}^{-2/3}$  ( $\tilde{\Omega}^{-1/3}$ ) at  $\omega = E_0$ . Thus, the physical spectral function  $\rho_{12}$  vanishes as  $|\omega|^{4/3}$  at the Fermi energy, while  $\rho_{01}$  is finite.

(2) Two-channel case:  $\gamma_c < 0$  or  $\epsilon_2 < 0$ . In contrast to the one-channel case, the  $f^2$  spectral function has a singular structure leading to two-channel ground state. The

integration constant and the Kondo temperature are

$$\frac{g_1}{T_0} = \exp\left[\frac{\pi(g_2 - g_1)}{2\Gamma}\right] \left[1 + \frac{g_2}{|\epsilon_2|}\right]^{1/2} \frac{g_2}{\Delta},\tag{58}$$

$$T_0 = D \left[ \frac{|\epsilon_2|}{D} \right]^{1/2} \left[ \frac{\Gamma}{\pi D} \right] \exp \left[ \frac{\pi(\epsilon_1 - \epsilon_2)}{2\Gamma} \right]. \tag{59}$$

Note that the Kondo temperature vanishes with  $\epsilon_2 \to 0$ . We can find the asymptotic behavior following the standard zero temperature analysis.

$$g_0(\omega) = g_2(\omega) + |\epsilon_2|,\tag{60}$$

$$\frac{g_1(\omega)}{T_0} = \tilde{\Omega}^{1/2} \left[ 1 + c_1 \tilde{\Omega}^{1/2} + \mathcal{O}(\tilde{\Omega}) \right], \tag{61}$$

$$\frac{g_2(\omega)}{\Delta} = \tilde{\Omega}^{1/2} \left[ 1 + c_2 \tilde{\Omega}^{1/2} + \mathcal{O}(\tilde{\Omega}) \right], \tag{62}$$

$$\tilde{\Omega} = 4 \frac{E_0 - \omega}{T_0},\tag{63}$$

$$c_1 = \frac{1}{6} \left[ 2 \left( 1 + \frac{\Delta}{|\epsilon_2|} \right) - \frac{T_0}{\Delta} \right]; \quad c_2 = -\frac{1}{6} \left[ \left( 1 + \frac{\Delta}{|\epsilon_2|} \right) - 2 \frac{T_0}{\Delta} \right]. \tag{64}$$

The asymptotic behavior above the ground state energy  $E_0$  can be obtained from the expressions below  $E_0$  by the analytic continuation. Furthermore, we find for the "negative frequency" spectra that

$$\frac{d}{d\tilde{\Omega}}a_0g_0^2 = \frac{T_0\Delta}{2} a_1,\tag{65}$$

$$\frac{d}{d\tilde{\Omega}}a_1g_1^2 = \frac{T_0\Delta}{2} \left[ \frac{1}{2}a_0 + a_2 \right], \tag{66}$$

$$\frac{d}{d\tilde{\Omega}}a_2g_2^2 = \frac{T_0\Delta}{2} a_1,\tag{67}$$

which implies for  $|\omega - E_0| \ll T_0$ 

$$a_0 = \frac{\Delta}{4|\epsilon_2|^2} \tilde{\Omega}^{1/2} \left[ 1 - x_0 \tilde{\Omega}^{1/2} + \mathcal{O}(\tilde{\Omega}) \right], \tag{68}$$

$$a_1 = \frac{1}{4T_0} \tilde{\Omega}^{-1/2} \left[ 1 - x_1 \tilde{\Omega}^{1/2} + \mathcal{O}(\tilde{\Omega}) \right], \tag{69}$$

$$a_2 = \frac{1}{4\Delta} \tilde{\Omega}^{-1/2} [1 - x_2 \tilde{\Omega}^{1/2} + \mathcal{O}(\tilde{\Omega})],$$
 (70)

$$x_0 = \frac{2}{3}(2c_1 + c_2) + 2\frac{\Delta}{|\epsilon_2|} = \frac{1}{3}\left(1 + \frac{7\Delta}{|\epsilon_2|}\right),$$
 (71)

$$x_1 = \frac{4}{3}(2c_1 + c_2) = \frac{2}{3}\left(1 + \frac{\Delta}{|\epsilon_2|}\right),$$
 (72)

$$x_2 = \frac{4}{3}(c_1 + 2c_2) = \frac{2}{3} \frac{T_0}{\Delta}.$$
 (73)

Note that  $x_{0,1,2} > 0$ . Now we can find the asymptotic behavior of the pseudo particle spectral functions.

$$A_0(\omega) = \frac{\Delta}{\pi |\epsilon_2|^2} \theta(\omega - E_0) \left[ |\tilde{\Omega}|^{1/2} + \mathcal{O}(|\tilde{\Omega}|^{3/2}) \right], \tag{74}$$

$$A_1(\omega) = \frac{1}{\pi T_0} \theta(\omega - E_0) \left[ |\tilde{\Omega}|^{-1/2} + \mathcal{O}(|\tilde{\Omega}|^{1/2}) \right], \tag{75}$$

$$A_2(\omega) = \frac{1}{\pi \Delta} \theta(\omega - E_0) \left[ |\tilde{\Omega}|^{-1/2} + \mathcal{O}(|\tilde{\Omega}|^{1/2}) \right]. \tag{76}$$

As expected,  $A_0(\omega)$  vanishes at the threshold energy and does not develop any singular behavior. On the other hand,  $A_1(\omega)$  and  $A_2(\omega)$  are singular at the threshold energy. Finally the physical spectral functions are given by in the asymptotic limit.

$$\rho_{01}(\omega > 0) = \frac{\Delta}{32|\epsilon_2|^2} \left[ \tilde{\omega} - \frac{8x_0}{3\pi} \, \tilde{\omega}^{3/2} + \cdots \right],\tag{77}$$

$$\rho_{01}(\omega < 0) = \frac{\Delta}{32|\epsilon_2|^2} \left[ |\tilde{\omega}| - \frac{4x_1}{3\pi} |\tilde{\omega}|^{3/2} + \cdots \right], \tag{78}$$

$$\rho_{12}(\omega > 0) = \frac{1}{16\Delta} \left[ 1 - \frac{2x_1}{\pi} \sqrt{\tilde{\omega}} + \cdots \right], \tag{79}$$

$$\rho_{12}(\omega < 0) = \frac{1}{16\Delta} \left[ 1 - \frac{2x_2}{\pi} \sqrt{|\tilde{\omega}|} + \cdots \right], \tag{80}$$

$$\chi''(\omega) = \frac{\operatorname{sign}(\omega)}{16\Delta} \left[ 1 - \frac{2x_1}{\pi} \sqrt{|\tilde{\omega}|} + \cdots \right], \tag{81}$$

$$\tilde{\omega} = 4\frac{\omega}{T_0}.\tag{82}$$

 $\rho_{01}(\omega)$  vanishes at  $\omega = 0$  and increases as  $|\omega|$  near the fermi level. This spectral depletion at the fermi level is also confirmed in the finite temperature NCA calculation.  $\rho_{12}$  is peaked right at the fermi level and has more spectral weight below than above the fermi level since  $x_2 < x_1$  for  $T_0 < \Delta$ . The finite temperature NCA results also confirm this observation. The spectral functions become non-analytic at the Fermi level at zero temperature. Note that the dynamic magnetic susceptibility is step function like at  $\omega = 0$ , which is none other than marginal fermi liquid behavior [14]. From the asymptotic form of the zero temperature

spectral functions, we can infer the finite temperature dependence of the resistivity using the Kubo formula

$$\frac{1}{\rho(T)} = \frac{ne^2}{m} \int d\omega \tau(\omega) \left( -\frac{\partial f}{\partial \omega} \right). \tag{83}$$

For  $\omega, T \ll T_0$ , the relaxation rate for the conduction electron is approximately

$$\frac{1}{\tau(\omega)} \propto \rho_{12}(\omega, T). \tag{84}$$

Near the zero temperature, we may replace  $\rho_{12}(\omega, T)$  by our zero temperature one and find the  $\sqrt{T}$  temperature dependence. In fact one complication arises due to the angular averaging. Since the angular harmonics conjugate to  $\rho_{12}$  is positive definite, still the above simple argument applies. In the one-channel case, we cannot use this kind of simple argument to find the low temperature behavior of resistivity. The scaling dimensions agree with those from the conformal field theory approach.

We summarize the low temperature properties: (i) The atomic spectral function  $\rho_{12}$  is peaked right at the Fermi level independent of the occupancy, while  $\rho_{01}$  vanishes at  $\omega = 0$  and is depleted near the fermi level; (ii) The dynamic magnetic susceptibility is step function-like at zero frequency; (iii) The resistivity obeys the scaling behavior  $\rho(T) = \rho(0) \left[ 1 - a\sqrt{T/T_0} \right]$  near zero temperature. All these results will be shown consistent with numerical NCA calculations at finite temperatures.

(3) Three-channel case:  $\gamma_c = 0$  or  $\epsilon_2 = 0$ . In this case, the  $f^0$  and  $f^2$  configurations are equivalent asymptotically leading to three-channel ground state. The integration constant and the Kondo temperature are

$$\frac{g_1}{T_0} = \left[\frac{g_0}{\Delta}\right]^{3/2} \exp\left[\frac{\pi}{2\Gamma} \left(g_0 - g_1\right)\right],\tag{85}$$

$$T_0 \approx D \left[\frac{\Gamma}{\pi D}\right]^{3/2} \exp\left[\frac{\pi \epsilon_1}{2\Gamma}\right].$$
 (86)

See the Appendix for the detailed derivation of asymptotic behavior. This model case is not different from the analysis of the general overcompensated models. We simply list the asymptotic behavior here.

$$g_0(\omega) = g_2(\omega), \tag{87}$$

$$\frac{g_1(\omega)}{T_0} = \tilde{\Omega}^{3/5} \left[ 1 + c_1 \ \tilde{\Omega}^{2/5} + d_1 \ \tilde{\Omega}^{3/5} + \cdots \right], \tag{88}$$

$$\frac{g_2(\omega)}{\Delta} = \tilde{\Omega}^{2/5} \left[ 1 + c_2 \tilde{\Omega}^{2/5} + d_2 \, \tilde{\Omega}^{3/5} + \cdots \, \right], \tag{89}$$

$$\tilde{\Omega} = 5 \frac{E_0 - \omega}{T_0},\tag{90}$$

$$c_1 = \frac{2}{7}, \quad d_1 = -\frac{T_0}{8\Delta}; \quad c_2 = -\frac{1}{7}, \quad d_2 = \frac{T_0}{4\Delta}.$$
 (91)

The nagative spectral functions are

$$a_1(\omega) = \frac{1}{5T_0} \tilde{\Omega}^{-3/5} \left[ 1 - x_1 \tilde{\Omega}^{2/5} - y_1 \tilde{\Omega}^{3/5} + \cdots \right] \theta(\tilde{\Omega}),$$
 (92)

$$a_2(\omega) = \frac{1}{5\Delta} \tilde{\Omega}^{-2/5} \left[ 1 - x_2 \tilde{\Omega}^{2/5} - y_2 \tilde{\Omega}^{3/5} + \cdots \right] \theta(\tilde{\Omega}), \tag{93}$$

$$x_1 = 2c_1 = \frac{4}{7}, \quad y_1 = 0; \quad x_2 = 0, \quad y_2 = 2d_2 = \frac{T_0}{2\Delta}.$$
 (94)

And the pseudo particle spectral functions are

$$A_1(\omega) = \frac{\sin(3\pi/5)}{\pi T_0} |\tilde{\Omega}|^{-3/5} \left[ 1 - x_1 \cos(2\pi/5) |\tilde{\Omega}|^{2/5} + \cdots \right] \theta(-\tilde{\Omega}), \tag{95}$$

$$A_2(\omega) = \frac{\sin(2\pi/5)}{\pi\Delta} |\tilde{\Omega}|^{-2/5} \left[ 1 - y_2 \cos(2\pi/5) |\tilde{\Omega}|^{3/5} + \cdots \right] \theta(-\tilde{\Omega}).$$
 (96)

From the pseudo particle spectral functions, we can find the physical spectral functions in the asymptotic limit.

$$\rho_{01}(\omega) = \rho_{12}(-\omega),\tag{97}$$

$$\rho_{12}(\omega > 0) = \frac{\sin(2\pi/5)}{25\pi\Delta} \left[ B(2/5, 3/5) - x_1 B(3/5, 4/5) |\tilde{\omega}|^{2/5} \right]$$

$$-y_2 \cos(2\pi/5) B(2/5, 6/5) |\tilde{\omega}|^{3/5} + \cdots|,$$
 (98)

$$\rho_{12}(\omega < 0) = \frac{\sin(3\pi/5)}{25\pi\Delta} \left[ B(2/5, 3/5) - x_1 \cos(2\pi/5) B(3/5, 4/5) |\tilde{\omega}|^{2/5} \right]$$

$$-y_2 B(2/5, 6/5) |\tilde{\omega}|^{3/5} + \cdots ],$$
 (99)

$$\tilde{\chi}''(\omega) = \text{sign}(\omega) \frac{\sin(3\pi/5)}{25\pi T_0} [B(2/5, 2/5) |\tilde{\omega}|^{-1/5}]$$

$$-x_1 [1 + \cos(2\pi/5)] B(2/5, 4/5) |\tilde{\omega}|^{1/5} + \cdots],$$
 (100)

$$\tilde{\omega} = 5 \; \frac{\omega}{T_0}.\tag{101}$$

Here B(p,q) is the Beta function. The spectral functions become non-analytic at the Fermi level at zero temperature. One important observation is that the power laws agree with those obtained from the conformal field theory treatments for the overcompensated multichannel S=1/2 models. Since  $\rho_{01}$  and  $\rho_{12}$  are equivalent in the asymptotic limit, the angular functions are factored out in the conduction electron scattering time. Thus we can read off the power law of the resistivity,  $\alpha=2/5$ .

Again, the low temperature properties are summarized below. (i) The atomic spectral function is peaked right at the Fermi level independent of the occupancy; (ii) The dynamic magnetic susceptibility diverges as  $\omega^{-1/5}$  at zero frequency; (iii) The resistivity obeys the scaling behavior  $\rho(T) = \rho(0) \left[ 1 - a(T/T_0)^{0.4} \right]$  near zero temperature. All these results will be shown consistent with numerical NCA calculations at finite T.

#### B. Crossover physics.

We expect the smooth crossover from the high temperature regime to the low temperature regime where the relevant channel number physics shows up. We can estimate the crossover temperature in the one- and two-channel model parameter regime using the zero temperature analysis. Noting that the asymptotic analysis assumes  $g_0 \ll \epsilon_2$  for the one-channel regime and  $g_2 \ll |\epsilon_2|$  for the two-channel regime (see the integration constant), we can estimate the crossover energy scale below which one- or two-channel physics is realized. In the one-channel case, the integration constant can be rewritten as

$$\frac{g_1}{T_0^{(3)}} = \left[1 + \frac{\epsilon_2}{g_0}\right] \left[\frac{g_0}{\Delta}\right]^{3/2} \exp\left[\frac{\pi(g_0 - g_1)}{2\Gamma}\right]. \tag{102}$$

We can see that the relative magnitude of  $g_0$  and  $\epsilon_2$  determines the differing channel behavior. The crossover energy scale can be defined by the relation  $g_0 = \epsilon_2$ . The crossover temperature is found in the one-channel case

$$T_{\mathbf{x}}^{(1)} = \frac{T_0}{3} \left[ \frac{\epsilon_2}{\Delta} \right]^{3/2}. \tag{103}$$

And in the two-channel case, we find the crossover temperature

$$T_{\mathbf{x}}^{(2)} = \frac{T_0}{4} \left[ \frac{|\epsilon_2|}{\Delta} \right]^2. \tag{104}$$

Substituting the Kondo energy scale, we can see that the crossover energy scales are

$$T_{\mathbf{x}}^{(1)} = \frac{1}{3} \left[ \frac{\epsilon_2}{\Delta} \right]^{5/2} D \left[ \frac{\Gamma}{\pi D} \right]^{3/2} \exp \left[ \frac{\pi \epsilon_1}{2\Gamma} \right], \tag{105}$$

$$T_{\mathbf{x}}^{(2)} = \frac{1}{4} \left[ \frac{|\epsilon_2|}{\Delta} \right]^{5/2} D \left[ \frac{\Gamma}{\pi D} \right]^{3/2} \exp \left[ \frac{\pi(\epsilon_1 - \epsilon_2)}{2\Gamma} \right]. \tag{106}$$

Note that the crossover temperature vanishes as  $|\epsilon_2|^{5/2}$  with  $\epsilon_2 \to 0$ . We intentionally write the crossover temperature as the prefactor times the corresponding three-channel Kondo temperature. If this prefactor is greater than 1, the system will not display the three-channel behavior with decreasing temperatures but will flow directly to the one- or two-channel fixed point. When this prefactor is less than 1, the system will display the three-channel behavior before finally flowing to each channel fixed point. In the one-channel regime, the system flows directly from the high temperature regime (local moment regime) to the one-channel fixed point when  $\epsilon_2 >> \Delta$  with decreasing temperatures. In the opposite limit,  $\epsilon_2 << \Delta$ , the system will flow from the local moment regime to the three-channel regime, and finally to the one-channel fixed point after passing through the crossover temperature. In the two-channel regime the same argument can be applied as in the one-channel case.

#### C. General asymmetric hybridization case.

Though the Kondo energy scale can not be estimated analytically for the general case  $\Gamma_{01} \neq \Gamma_{12}$ , still the asymptotic behavior ( $\omega \leq E_0$ ) can be sorted out. Since the physics is the same as the above analysis, we shall just write the asymptotic properties of Green's functions.

(1)  $\gamma_c > 0$ :

$$g_0(\omega) \approx \frac{\Gamma_{01}}{\pi} \left[ 3 \frac{E_0 - \omega}{T_0} \right]^{\alpha_0}, \tag{107}$$

$$g_1(\omega) \approx T_0 \left[ 3 \frac{E_0 - \omega}{T_0} \right]^{\alpha_1},$$
 (108)

$$g_2(\omega) = \frac{\Gamma_{12}}{\Gamma_{01}} g_0(\omega) + \left[ \frac{\Gamma_{12}}{\Gamma_{01}} - 1 \right] (\omega - E_0) + \gamma_c \Gamma_{12}, \tag{109}$$

$$\alpha_0 = \frac{2}{3}; \quad \alpha_1 = \frac{1}{3}.$$
 (110)

(2)  $\gamma_c < 0$ :

$$g_0(\omega) = \frac{\Gamma_{01}}{\Gamma_{12}} g_2(\omega) + \left[ \frac{\Gamma_{01}}{\Gamma_{12}} - 1 \right] (\omega - E_0) + |\gamma_c| \Gamma_{01}, \tag{111}$$

$$g_1(\omega) \approx T_0 \left[ 4 \frac{E_0 - \omega}{T_0} \right]^{\alpha_1}, \tag{112}$$

$$g_2(\omega) \approx \frac{\Gamma_{12}}{\pi} \left[ 4 \frac{E_0 - \omega}{T_0} \right]^{\alpha_2},\tag{113}$$

$$\alpha_1 = \frac{1}{2}; \quad \alpha_2 = \frac{1}{2}.$$
 (114)

(3)  $\gamma_c = 0$ : In this case,  $f^0$  and  $f^2$  are equivalent asymptotically.

$$g_2(\omega) = \frac{\Gamma_{12}}{\Gamma_{01}} g_0(\omega) + \left[ \frac{\Gamma_{12}}{\Gamma_{01}} - 1 \right] (\omega - E_0)$$
 (115)

$$\frac{d}{d\omega}g_0(\omega) = -1 - \frac{2\Gamma_{01}}{\pi} \frac{1}{g_1(\omega)}; \quad g_0(-D) = D,$$
(116)

$$\frac{d}{d\omega}g_1(\omega) = -1 - \frac{\Gamma_{01}}{\pi} \left[ \frac{1}{g_0(\omega)} + \frac{2}{g_0(\omega) + (1 - \Gamma_{01}/\Gamma_{12})(\omega - E_0)} \right]; \quad g_1(-D) = D + \epsilon_1. \quad (117)$$

Then the asymptotic form follows

$$g_0(\omega) \approx \frac{\Gamma_{01}}{\pi} \left[ 5 \frac{E_0 - \omega}{T_0} \right]^{\alpha_0},$$
 (118)

$$g_1(\omega) \approx T_0 \left[ 5 \frac{E_0 - \omega}{T_0} \right]^{\alpha_1}, \tag{119}$$

$$\alpha_0 = \frac{2}{5}; \quad \alpha_1 = \frac{3}{5}.$$
 (120)

Though the Kondo energy scale cannot be evaluated analytically, it can be estimated from the numerical NCA calculation of, e.g., magnetic susceptibility and fitting it onto the universal results.

#### V. NUMERICAL ANALYSIS.

In this section we present results from our full numerical study at finite temperatures. We studied the model for the parameters listed in Table C 2. This covers the one-, two-, and three-channel Kondo regimes. For simplicity, we have chosen the same hybridization strength in the  $f^0 - f^1$  and the  $f^1 - f^2$  sectors. The relevant channel-number-dependent physics can then be studied by varying the relative position of the  $f^0$  and the  $f^2$  configuration energies. This simple choice of the hybridization further makes it possible to find the characteristic Kondo energy scales analytically, which is described in the previous section in detail.

Our main results are: (1) The magnetic susceptibility shows a scaling behavior and agrees well with the exact Bethe ansatz results in the two- and three-channel parameter regimes; (2) The NCA results of residual entropy in the two-, and three-channel models agree with the exact ones within order  $\mathcal{O}(1/N)$ . The Kondo anomaly peak in the specific heat also agrees with the exact one in its magnitude; (3) The thermopower is a diagnostic to display the ground states for different numbers of relevant channels for our model; (4) The dynamic magnetic susceptibility is distinct between the one-channel model and overcompensated (two- and three-channel) models; (5) Due to the simplifying features of our model, the resistivity shows a bendover at low temperatures in the one-channel parameter regime. The resistivity in the two- and three-channel parameter regimes shows temperature dependences near T = 0K agreeing with the conformal field theory results; (6) We confirmed in detail that NCA is a valid numerical self-consistent non-perturbative method in studying the overcompensated multi-channel  $S_I = 1/2$  Anderson model at T > 0.

#### A. Entropy and specific heat.

The entropy and the specific heat due to the magnetic impurity can be calculated from the free energy obtained in NCA through numerical differentiation. These thermodynamic quantities include very important information about the nature of the ground state. We can estimate the characteristic energy scales in the Kondo models from the temperature variation of the entropy. In general, the entropy will increase with increasing temperatures, until the frozen impurity degrees of freedom are released. Our model Hamiltonian is expected to have the entropy  $S = k_B \ln 5$  at high enough temperatures, while the residual entropy at zero temperature will show behavior expected for different numbers of relevant channels.

The entropy and the specific heat are displayed in Fig. 6 and 7 for the model parameter sets studied here. In the one-channel case, the Kondo anomaly peak is well separated from the Schottky anomaly peak coming from the interconfiguration excitations. The Kondo anomaly peak has a magnitude comparing well with the exact results [13] for the Kondo exchange model. No residual entropy remains with  $T \to 0$ . In the two-channel case, the Kondo anomaly peak is not clearly separated from the charge fluctuation peak for most of our model parameters. The residual entropy agrees within 5 % with the exact one [13] and the discrepancy can be explained by the  $\mathcal{O}(1/N^2)$  and higher order corrections. To see this, we note that the entropy for spin 1/2 conduction electrons has an explicit dependence on the impurity spin degeneracy [8,9]. Strictly speaking, the NCA results are valid for Nfold impurity spin and M-fold channel degeneracies as  $N \to \infty$  with N/M fixed. Hence it is natural to expect  $\mathcal{O}(1/N^2)$  corrections to the entropy through the neglected vertex corrections. In the three-channel case, the Kondo anomaly peak is reduced further due to the increased residual entropy and is almost merged with the charge fluctuation contribution for model set 4. For model set 5, we can see a weak indication of separation. The residual entropy is increased compared to that of two-channel case and its magnitude is again a little bit smaller than the exact one [13] due to the neglect of the higher order contribution in 1/N expansion.

#### B. Static magnetic susceptibility.

The static magnetic susceptibility is a direct indicator of the nature of the ground state for the magnetic Kondo model. As is well documented, the magnetic susceptibility diverges logarithmically  $\chi(T) \propto \log(T_0/T)$  for the two-channel  $S_I = 1/2$  magnetic Kondo model at zero temperature, and diverges algebraically for the three or the higher channel  $S_I = 1/2$  Kondo model  $(\chi(T) \propto [T_0/T]^{1-2\Delta_n}$ ;  $\Delta_n = 2/(n+2)$ : n is the channel number  $(\geq 3)$  [8,9,13]. The one-channel Kondo model has a constant magnetic susceptibility at zero temperature  $(\chi(0) \sim 1/T_0)$ . From the NCA, using the leading order bubble diagram [6], the magnetic susceptibility for one Ce<sup>3+</sup> impurity is given by

$$\chi(T) = \frac{1}{3}\mu_{\text{eff}}^2 \tilde{\chi}(T), \quad \mu_{\text{eff}}^2 = \frac{75}{49}\mu_{\text{B}}^2,$$
(121)

$$\tilde{\chi}(T) = -\frac{4}{Z_{\rm f}} \int d\zeta \ a_1(\zeta, T) \ \text{Re}G_1(\zeta, T). \tag{122}$$

Here  $\mu_{\rm B}$  is the Bohr magneton.

Our numerical results for  $\tilde{\chi}(T)$  clearly show the right tendency for each possible low T channel number. The magnetic susceptibility in the one-channel regime, for the model parameter sets 6, 7, 8 shows approximate scaling behavior and clearly has the negative curvature at low temperatures indicating approach to the Fermi liquid ground state. The deviation of the scaling behavior at low temperatures seems to come from the pathological behavior of NCA in this one-channel case [44].

The  $\tilde{\chi}(T)$  curves in the two-channel regime, for the model parameter sets 1, 2, 3, also show scaling behavior and diverge logarithmically at low temperatures (Fig. 8). Our results are compared with those of Ref. [13]. The fitting to the exact Bethe ansatz numerical results [13] is quite good. We believe that the high temperature deviation comes from the M=3 to M=2 crossover physics described in the previous section. Note that Bethe ansatz results are for the pure two-channel s-d exchange model. To get the fitting to the Bethe ansatz, we slide the temperature axis to find  $T_K=0.3\times T_0$  ( $T_K$  from the Bethe Ansatz). Here  $T_0$  is the Kondo energy scale estimated from the zero temperature analysis.

At high temperatures we cannot distinguish the different numbers of relevant channels clearly. Note that distinct physics for different numbers of relevant channels shows up at low temperatures below the crossover temperature which was estimated in the previous section. This observation is supported by results from the three-channel model parameter sets. The high temperature deviation from scaling is very weak in this case which will not show the crossover physics. The magnetic susceptibility in the three-channel model also shows a scaling behavior. Since the three-channel case lies exactly on the boundary between the one-channel and the two-channel regime, we probed the three-channel case by varying the position of the bare  $f^1$  configuration energy while the two excited configurations  $f^0$ ,  $f^2$  energies are kept equal. Fitting to the exact results is quite good. The Kondo energy scale  $T_0$  estimated from the zero temperature analysis agrees with that in the exact Bethe ansatz  $(T_K \text{ of Ref } [13])$ .

#### C. Spectral functions.

The interconfiguration spectral functions show a distinct behavior for different numbers of relevant channels near the the Fermi level ( $\omega = 0$ ) depending on the model parameters. In our simple model, we have two symmetry atomic spectral functions of  $\Gamma_7$  and  $\Gamma_8$ :  $\rho_{\Gamma_7}(\omega) = \rho_{01}(\omega)$  and  $\rho_{\Gamma_8}(\omega) = \rho_{12}(\omega)$ .

$$\rho_{01}(\omega) = \frac{1 + e^{-\beta\omega}}{Z_f} \int d\zeta \ e^{-\beta\zeta} \ A_0(\zeta) \ A_1(\zeta + \omega) \tag{123}$$

$$\rho_{12}(\omega) = \frac{1 + e^{-\beta\omega}}{Z_{\rm f}} \int d\zeta \ e^{-\beta\zeta} \ A_1(\zeta) \ A_2(\zeta + \omega) \tag{124}$$

In the one-channel model parameter regime (see Fig. 9),  $\rho_{01}(\omega)$  develops the Kondo resonance peak just above the Fermi level and  $\rho_{12}(\omega)$  is depleted near  $\omega = 0$  and tends to zero with  $T \to 0$  at  $\omega = 0$ . This confirms our zero temperature analysis in section IV. For comparison, note that the Kondo resonance amplitude is big compared to the two-channel or three-channel cases.

In the two-channel regime (see Fig. 10),  $\rho_{12}(\omega)$  is peaked below  $\omega = 0$  and its peak position tends to  $\omega = 0$  with decreasing temperature. Note that the Kondo resonance amplitude is reduced compared to the one-channel Kondo resonance amplitude. On the other hand,  $\rho_{01}(\omega)$  is depleted near  $\omega = 0$ .

In the three-channel parameter regime (see Fig. 11), the two spectral functions are equivalent asymptotically when  $\omega \to -\omega$  transformation is accounted for. Peak positions tend to zero with decreasing temperature. Both develop the Kondo resonance peak with further reduced amplitude.

As mentioned above, the positions of the Kondo resonance peak (see Fig. 12) show a distinct behavior for different numbers of relevant channels. The peak position saturates to a constant value in the one-channel cases while it vanishes in the two- and three-channel cases with decreasing temperature. In addition, the detailed functional forms of the Kondo resonance peak are different depending on the relevant channel numbers. In the overscreened cases (M = 2, 3), the peak structure becomes non-analytic with decreasing temperature as shown in the zero temperature analysis of the NCA integral equations. Finite temperature washes out this non-analytic behavior at the Kondo resonance peak. In the one-channel case, the atomic spectral functions remain analytic down to zero temperature.

Since we are not considering all the atomic energy levels, the full atomic spectral functions (measured from the photoemission experiments) cannot be defined in our simple model. Though the high energy physics of real systems can not be properly treated within our simple model Hamiltonian, the low energy or low temperature properties can be studied using the restricted spectral functions. Note that low temperature/energy physics is governed by the Kondo resonance peak development. Though the spectral depletion is found in the interconfiguration spectral functions, we do not expect that the photoemission spectroscopy can observe this feature unless it can distinguish the atomic electron symmetry. Measurable atomic spectral functions are shown in Fig. 13 for each relevant channel case.

#### D. Dynamic magnetic susceptibility.

The dynamic magnetic susceptibility measures the magnetic excitation structure. Since the properties of the magnetic excitations are related to the interaction of the local magnetic moment with the conduction electrons, the relevant channel number will determine the nature of the magnetic excitations. The dynamic magnetic susceptibility is expected to be distinct for each number of relevant channels. We have already seen this channel dependence in the static magnetic susceptibility.

Dynamic magnetic susceptibility is defined as the spin-spin correlation function and can be measured directly from the neutron scattering experiments. From the leading bubble diagram, the reduced dynamic magnetic susceptibility is

$$\tilde{\chi}''(\omega, T) = \frac{1 - e^{-\beta \omega}}{Z_{\rm f}} \int d\zeta \ a_1(\zeta, T) \ A_1(\zeta + \omega, T). \tag{125}$$

Our reduced static magnetic susceptibility is related to the above magnetic response function by the Kramer-Kronig relation:

$$\tilde{\chi}(T) = 2 \int \frac{d\omega}{\pi} \frac{\tilde{\chi}''(\omega, T)}{\omega}.$$
 (126)

The neutron scattering experiments measure the structure function  $S(\omega,T) \propto [b(\omega) + 1] \chi''(\omega,T)$ . The dynamic susceptibility can be quantitatively characterized by its 'linewidth' dependence on temperature in addition to its overall functional shape. We may define the linewidth  $\Gamma(T)$  by the peak position of  $\chi''(\omega,T)$ , which can be measured directly in the inelastic neutron scattering experiments.

The variation of  $\chi''(\omega, T)$  and  $\Gamma(T)$  with temperature are displayed in Fig. 14 and 15. For the dynamic magnetic susceptibility, we display the reduced form  $\tilde{\chi}''(\omega, T)/\tilde{\chi}''(\Gamma(T), T)$  as a function of  $\omega/\Gamma(T)$ . The distinct behavior for different number of relevant channels is clearly evidenced: in the one-channel regime, the  $\tilde{\chi}''(\omega, T)$  curves converge with decreasing temperatures (not shown). This is clearly supported by the saturation of  $\Gamma(T)$  at low temperatures. In the two- and three-channel regimes,  $\Gamma(T)$  vanishes algebraically (close to linear) and the dynamic magnetic susceptibility does not converge (not shown) in contrast to the one-channel case, but instead develops non-analytic behavior at  $\omega=0$ . The reduced dynamic magnetic susceptibilities (defined above, see Fig. 14) roughly show a scaling behavior between two extrema.

The physics of the linewidth is quite important in understanding the nature of the magnetic spin screening. The distinct behavior for different numbers of channels shows up at low temperatures below  $T_0$ . The impurity spin flipping time ( $\tau_f$ ) due to the hybridization will be given by the inverse of the linewidth,  $\tau_f \sim 1/\Gamma(T)$ . On the other hand, thermally excited conduction electrons close to the impurity site will pass through it in a time  $\tau_c$  of order of 1/T from the uncertainty principle. At high temperatures above the Kondo temperature,  $\tau_f \gg \tau_c$ . Thus the impurity spin rarely flips while the conduction electrons pass by the impurity site. Hence the Curie behavior is expected in the magnetic susceptibility. At low temperatures below the Kondo temperature, differing channel number physics shows up. In the one-channel regime,  $\tau_f \ll \tau_c$  and the impurity spin flips vigorously averaging out its spin to zero and leading to the Pauli behavior. In the two- and three-channel regimes,  $\tau_f \approx \tau_c$  and spin screening is not complete leading to the non-Fermi liquid ground state. This interpretation agrees with the low temperature behaviors of magnetic susceptibility.

#### E. Transport coefficients.

Using the Kubo formula [6] in a dilute impurity limit, where the inter-impurity correlation can be neglected, we have calculated the transport coefficients, resistivity and thermopower. The anisotropic conduction electron scattering rate is

$$\tau^{-1}(\hat{k},\omega) = \frac{8\pi n_{\text{imp}}}{N(0)} \left[ \Gamma_{01} \Theta_7^{(5/2)}(\hat{k}) \rho_{01}(\omega) + \Gamma_{12} \Theta_8^{(5/2)}(\hat{k}) \rho_{12}(\omega) \right], \tag{127}$$

$$\Theta_7^{(5/2)}(\hat{k}) = \frac{1}{16\pi} \left[ 6 - \Phi(\hat{k}) \right]; \quad \Theta_8^{(5/2)}(\hat{k}) = \frac{1}{16\pi} \left[ 6 + \Phi(\hat{k}) \right], \tag{128}$$

$$\Phi(\hat{k}) = 15\cos^4\theta - 10\cos^2\theta + 1 + 5\sin^4\theta\cos^22\varphi.$$
 (129)

Here  $n_{\rm imp}$  is the impurity concentration. Note that the conduction electron scattering rate contains the hybridization since the interconfiguration spectral functions are involved. The crystal harmonics are normalized such that the integration of  $\Theta_7^{(5/2)}(\hat{k})$  and  $\Theta_8^{(5/2)}(\hat{k})$  over the solid angle leads to 1 and 2, respectively. Note that the the crystal harmonic  $\Theta_7^{(5/2)}(\hat{k})$  vanishes at "hot spot" angles of  $(\theta, \varphi) = (0, -), (\pi, -), (\pi/2, 0), (\pi/2, \pi/2), (\pi/2, \pi), (\pi/2, 3\pi/2),$  while  $\Theta_8^{(5/2)}(\hat{k})$  is positive definite. This feature, combined with the dip structure of the interconfiguration spectral function  $(f^1 - f^2)$  or  $\rho_{\Gamma_8}(\omega)$ , leads to a bendover in resistivity at low

temperatures in the one-channel parameter regime within our simplified model. We believe this feature will go away in more realistic models. For example, another contribution to the  $\Gamma_8$  atomic spectral function comes from the convolution between  $f^0$  and  $f^1$  J=5/2  $\Gamma_8$ . This spectral function will not be depleted at the fermi level, but instead will build up its spectral weight due to the weak Kondo resonance structure just above  $\omega=0$ . Thus the low temperature bendover in the resistivity will disappear.

The channel-dependence of the spectral functions, combined with the angular dependence, leads to a distinct behavior in the angle-averaged conduction electron lifetime for different numbers of channels. The spectral depletion becomes pronounced in the one-channel regime due to the angular average over the  $\Gamma_7$  "hot spots." The development of the dip structure just below the Fermi level is correlated to the resistivity bendover at low temperatures. This feature does not occur in the two- and three-channel regimes. A Kondo resonance related peak develops near the Fermi energy, whose position with respect to the Fermi level depends on the channel character of the model parameters. Details are displayed in Fig. 16. Note that the anisotropic scattering rate includes explicitly the hybridization as opposed to the other spectral functions like the atomic electron spectral function and the dynamic susceptibility.

The transport coefficients are calculated using the Kubo formula under the assumption of dominant scattering in the l=3 channel. Our results are defined in terms of transport integrals  $I_n$  given by equations.

$$I_n(T) = \int d\omega \ \omega^n \ \tau(\omega, T) \left[ -\frac{\partial f(\omega)}{\partial \omega} \right], \tag{130}$$

$$\tau(\omega, T) \equiv \int \frac{d\hat{k}}{4\pi} \, \tau(\hat{k}, \omega, T). \tag{131}$$

Here  $f(\omega)$  is Fermi function. The resistivity is calculated using the equation:

$$\frac{1}{\rho(T)} = \frac{ne^2}{m} I_0(T). \tag{132}$$

As we stated before, the resistivity shows a bendover at low temperatures in the onechannel regime within our simple model (not shown). This derives from the depleted spectral weight in the  $f^1 - f^2$  sector and zeros of  $\Theta_7^{(5/2)}(\hat{k})$ .

In the two-channel and three-channel model parameter regimes, the resistivity initially increases logarithmically through  $T_0$  and then saturates with a power law to a constant with further decreasing temperatures. The resistivity near zero temperature obeys a scaling behavior as shown in Fig. 17 confirming our zero temperature analysis with the scaling dimensions,  $\Delta_2 = 1/2$ ,  $\Delta_3 = 2/5$ . These results agree with the conformal field theory results [8,9],  $\rho(T) = \rho(0)$  [  $1 - a[T/T_0]^{\Delta_n}$  ] for  $T \leq 0.06T_0$ ,  $\Delta_n = 2/(n+2)$  for the overcompensated multi-channel Kondo models (note that the power law exponent is independent of the impurity spin size). We note that the region where strict  $T^{\Delta_n}$  behavior holds is below about 0.05  $T_0$ . A fit to the resistivity of  $Ce_xLa_{1-x}Cu_{2.2}Si_2$  (see Fig. 1) is good until low temperatures where the data breaks below theory. This suggests a possible crossover to a new fixed point which could be set by intersite interactions (producing a spin molecular field) or a weak noncubic symmetry for the  $Ce^{3+}$  ions.

The thermopower is a sensitive measure of the asymmetry in the scattering rate and the density of states (DOS) near the Fermi level. Since we are assuming the symmetrical Lorentzian/Gaussian DOS for the conduction band, the sign of the thermopower is determined by the asymmetrical scattering rate.

$$Q(T) = -\frac{1}{eT} \frac{I_1(T)}{I_0(T)}. (133)$$

As shown in Fig. 18, the thermopower shows explicitly the distinct behavior for different numbers of channels varying from the two-channel regime, through the three-channel, finally to the one-channel regime. The hybridization between  $f^0$  and  $f^1$  leads to the Kondo resonance peak just above the Fermi level and more spectral weight above the Fermi level. Since particle scattering dominates, holes are the main carriers in the one-channel cases, thus leading to a positive thermopower. On the other hand, negative thermopower arises in the  $f^1 - f^2$  sector. In this case, hole scatterings dominate and particles are the main carriers. In the three-channel regime, energy structures are symmetric. However, the double degeneracy in the  $f^2$  configuration leads to a weak hole scattering dominance resulting in a

negative thermopower at low temperatures. The overall magnitude of the thermopower is slightly reduced when anisotropy at the cubic sites is included.

#### VI. DISCUSSION AND CONCLUSION

We have introduced and studied a realistic model Hamiltonian for  $Ce^{3+}$  impurities with three configurations  $(f^0, f^1, f^2)$ , which are embedded in cubic normal metals. This simple model shows competition between the Fermi liquid fixed point of the one-channel S = 1/2Kondo model and the non-Fermi liquid fixed point of the two-channel S = 1/2 Kondo model.

We studied a simplified Anderson model using the NCA. This simple model covers one-, two-, and three-channel Kondo physics depending on the model parameters. All the calculated physical quantities show the signatures of the Kondo effect appropriate to the different numbers of relevant channels. The magnetic susceptibility agrees with the exact Bethe Ansatz results for the two- and three-channel model parameter regime and has the correct scaling dimension agreeing with the conformal field theory results. Entropy and specific heat calculations also agree with the Bethe ansatz results within  $\mathcal{O}(1/N^2)$  approximation. Though the resistivity in the one-channel regime bends over with decreasing temperatures, we do not believe that this feature will survive when all the energy level structures, especially  $f^1J = 5/2\Gamma_8$ , are included. In the two- and three-channel parameter regimes, the resistivity increases logarithmically and saturates with decreasing temperatures. The low temperature behavior leads to power laws in agreement with the conformal field theory results.

Since the thermopower is very sensitive to the density of states structure and the scattering mechanism near the Fermi level, its sign and its magnitude depend on which fixed point is stable at zero temperature. In the one-channel regime, electrons are strongly scattered due to the Kondo resonance above the Fermi level and the thermopower remains positive definite and large due to the resonant scattering. In the two-channel case, holes are scattered off the impurity sites stronger than electrons. Thus electrons are the main carriers leading to the negative thermopower. In the three-channel regime, though hole scattering

is reduced compared to the two-channel case, electrons are still the main carriers due to the degeneracy imbalance between the singlet  $f^0$  and the doublet  $f^2J=4\Gamma_3$ . The thermopower remains negative with reduced value. We calculated the dynamic magnetic susceptibility and characterized it with its peak position  $(\Gamma(T))$  as a function of temperature. We can see the clear difference between one-channel and the overcompensated cases. While  $\Gamma(T)$  decreases and saturates to a constant value of order  $T_K$  with decreasing temperatures in the one-channel case,  $\Gamma(T)$  goes to zero almost linearly with decreasing temperatures in the two- and three-channel case.

We now discuss the experimental relevance of our model study to the  $Ce_{1-x}La_xCu_{2,2}Si_2$  alloy [17]. We already stressed the experimental evidences supporting the two-channel Kondo effect in this alloy system in the section I. The thermopower for  $CeCu_2Si_2$  changes sign around 70 K and is negative and large below [18,45]. As our numerical calculation shows, the thermopower is negative and large in the two-channel regime. This result compares well with the experimental findings for the stoichiometric system with x = 1. We believe the sign change comes from the Kondo resonance of  $f^0$  and  $f^1\Gamma_8$ , which lies above the Fermi level. Further experiments are required for the alloy system with excess Cu. For comparison, we note that  $CeAl_2$  or  $CeAl_3$  [45] have a positive thermopower large compared to transition metals at high temperatures and have a sign change at low temperature which is still bigger than the Kondo temperature. Our thermopower calculation and the thermopower dependence on the unit cell volume [46] suggests that the alloy system  $Ce_{1-x}La_xCu_{2,2}Si_2$  can go through the three-channel model parameter regime with external pressure. Renormalized atom calculations further suggest a destabilization of  $f^2$  relative to  $f^0$  with initial increasing pressure [47].

In addition to the thermopower, the future neutron scattering experiments for  $Ce_{1-x}La_xCu_{2.2}Si_2$  alloy can search for the dependence of  $\Gamma(T)$  (the peak position of the dynamic magnetic susceptibility) consistent with our proposal for the channel number.

#### ACKNOWLEDGMENTS

This research was supported by a grant from the U.S. Department of Energy, Office of Basic Energy Sciences, Division of Materials Research. We thank Eunsik Kim for her careful reading of this paper and thank L. N. Oliveira and J.W. Wilkins for stimulating interactions.

# APPENDIX A: NCA SELF ENERGY IN THE PRESENCE OF MULTIPLE, SAME IRREPS

In the  $f^2$  configuration, there are 9 irreducible representations of  $\Gamma_3$  in a cubic symmetry. NCA self energy diagrams should be generalized to get the right Kondo energy scale. As an example, we may consider the mixing process between  $f^1J=5/2\Gamma_7$  and  $f^2\Gamma_3$ 's. The relevant NCA integral equations are

$$\Sigma(\omega) = \frac{2}{\pi} \sum_{ij} \sqrt{\Gamma_i \Gamma_j} \int d\epsilon \ f(\epsilon) \tilde{N}(\epsilon) \ D_{ij}(\epsilon + \omega), \tag{A1}$$

$$\Pi_{ij}(\omega) = \frac{2}{\pi} \sqrt{\Gamma_i \Gamma_j} \int d\epsilon \ f(-\epsilon) \tilde{N}(\epsilon) \ G(\epsilon + \omega). \tag{A2}$$

The conduction electrons of only  $\Gamma_8$  symmetry are involved in the mixing process. The  $f^2\Gamma_3$ 's Green's function now becomes a  $9 \times 9$  matrix. This generalization can be seen most clearly by looking at the self energy diagrams of  $f^2\Gamma_3$ 's. The incoming  $\Gamma_3$  does not need to be the same as the outgoing  $\Gamma_3$ . This leads to the matrix Green's function for  $f^2\Gamma_3$ 's.

According to the Schrieffer-Wolff transformation, the effective Hamiltonian is

$$H_1 = J \sum_{n} \vec{S}_I \cdot \vec{S}_{cn}(0); \quad J = \sum_{i=1}^{9} \frac{2|V_{12}^i|^2}{\epsilon_2^i - \epsilon_1}.$$
 (A3)

Now we can show that the above NCA integral equations lead to the right Kondo energy scale to leading order.

$$G(\omega) \to \frac{1}{\omega - \epsilon_1 + i\delta}.$$
 (A4)

With this replacement, the  $\Gamma_3$  self energy matrix becomes

$$\Pi_{ij}(\omega) = \frac{2}{\pi} \sqrt{\Gamma_i \Gamma_j} \log \left| \frac{\omega - \epsilon_1}{\omega - D - \epsilon_1} \right|$$
(A5)

for a symmetric flat conduction band DOS with a half width D. Now the Kondo energy scale is determined by

$$\det \left[ (\omega - \epsilon_2^i) \delta_{ij} - \Pi_{ij}(\omega) \right] = 0. \tag{A6}$$

With the substitution  $\omega = \epsilon_1 - T_0$ , we can find the following

$$\log\left|\frac{T_0}{D+T_0}\right| = \frac{1}{N(0)J},\tag{A7}$$

$$N(0)J = \frac{2}{\pi} \sum_{i=1}^{9} \frac{\Gamma_i}{\epsilon_2^i - \epsilon_1}.$$
 (A8)

Here  $\Gamma_i = \pi N(0) |V_{12}^i|^2$ .

In conclusion, we have shown that the inclusion of all the  $\Gamma_3$ 's in the  $f^2$  configuration leads to the enhanced two-channel exchange coupling.

# APPENDIX B: ZERO TEMPERATURE ANALYSIS: OVERCOMPENSATED MULTICHANNEL ANDERSON MODEL.

We discuss the following NCA integral equations at zero temperature.

$$G_{g}(z) = \frac{1}{z - \epsilon_{g} - \Sigma_{g}(z)}; \quad \Sigma_{g}(z) = \frac{N_{x}\Gamma}{\pi} \int d\epsilon \tilde{N}(-\epsilon) f(\epsilon) G_{x}(z + \epsilon), \tag{B1}$$

$$G_{\mathbf{x}}(z) = \frac{1}{z - \epsilon_{\mathbf{x}} - \Sigma_{\mathbf{x}}(z)}; \quad \Sigma_{\mathbf{x}}(z) = \frac{N_{\mathbf{g}}\Gamma}{\pi} \int d\epsilon \tilde{N}(\epsilon) f(\epsilon) G_{\mathbf{g}}(z + \epsilon). \tag{B2}$$

Here  $\tilde{N}(\epsilon)$  is the normalized DOS such that  $\tilde{N}(0) = 1$ . For definiteness, we assume that the excited state has one less electron than the ground state. Before diving into the zero temperature analysis, we point out the applicability of NCA approach to the Anderson impurity model. Whenever the ground and the excited states have degeneracies of  $N_{\rm g}$  and  $N_{\rm x}$ , respectively, the above form of NCA integral equations are obtained. The above NCA integral equations also derive from the  $N_{\rm x}$ -channel,  $S_I = (N_{\rm g} - 1)/2$  models. This is an artifact of the NCA approach. The NCA can not distinguish between these two different

models. Note that not all the Anderson models with the degeneracies of  $N_{\rm g}$  (the ground state) and  $N_{\rm x}$  (the excited state) map into the  $N_{\rm x}$ -channel,  $S_I = (N_{\rm g} - 1)/2$  models. The Schrieffer-Wolff transformation is essential to see this connection clearly. As an example, the excited triplets in the  $f^2J=4$  in our Ce<sup>3+</sup> model leads to the one-channel exchange interaction of the impurity  $f^1\Gamma_7$  pseudo spin  $S_I=1/2$  coupled to the  $S_c=3/2$  conduction electrons [34] instead of three-channel Kondo model. With this restriction in mind, we now study the zero temperature analysis of the above NCA integral equations [14,44].

The dynamical quantities we are interested in are

$$\rho(\omega) = \int d\epsilon \left[ a_{\mathbf{x}}(\epsilon) A_{\mathbf{g}}(\epsilon + \omega) + A_{\mathbf{x}}(\epsilon) a_{\mathbf{g}}(\epsilon + \omega) \right], \tag{B3}$$

$$\chi_{\rm g}''(\omega) = \int d\epsilon \left[ a_{\rm g}(\epsilon) A_{\rm g}(\epsilon + \omega) - A_{\rm g}(\epsilon) a_{\rm g}(\epsilon + \omega) \right], \tag{B4}$$

$$a_{\rm g}(\omega) \equiv \frac{e^{-\beta\omega}}{Z_{\rm f}} A_{\rm g}(\omega); \quad a_{\rm x}(\omega) \equiv \frac{e^{-\beta\omega}}{Z_{\rm f}} A_{\rm x}(\omega).$$
 (B5)

We can show that

$$a_{g}(\omega)|G_{g}(\omega)|^{-2} = \frac{N_{x}\Gamma}{\pi} \int d\epsilon \tilde{N}(-\epsilon)f(-\epsilon)a_{x}(\omega + \epsilon), \tag{B6}$$

$$a_{\mathbf{x}}(\omega)|G_{\mathbf{x}}(\omega)|^{-2} = \frac{N_{\mathbf{g}}\Gamma}{\pi} \int d\epsilon \tilde{N}(\epsilon) f(-\epsilon) a_{\mathbf{g}}(\omega + \epsilon).$$
 (B7)

At zero temperature, Fermi function is reduced to step function. Thus, the self energy equations are simplified:

$$\Sigma_{g}(z) = \frac{N_{x}\Gamma}{\pi} \int_{-\infty}^{0} d\epsilon \tilde{N}(-\epsilon) G_{x}(z+\epsilon),$$
 (B8)

$$\Sigma_{\mathbf{x}}(z) = \frac{N_{\mathbf{g}}\Gamma}{\pi} \int_{-\infty}^{0} d\epsilon \tilde{N}(\epsilon) G_{\mathbf{g}}(z+\epsilon), \tag{B9}$$

$$a_{\rm g}(\omega)|G_{\rm g}(\omega)|^{-2} = \frac{N_{\rm x}\Gamma}{\pi} \int_0^\infty d\epsilon \ \tilde{N}(-\epsilon)a_{\rm x}(\omega + \epsilon),$$
 (B10)

$$a_{\mathbf{x}}(\omega)|G_{\mathbf{x}}(\omega)|^{-2} = \frac{N_{\mathbf{g}}\Gamma}{\pi} \int_{0}^{\infty} d\epsilon \ \tilde{N}(\epsilon)a_{\mathbf{g}}(\omega + \epsilon). \tag{B11}$$

For a flat conduction band with cut-off, [-D, D], we can reduce the above equations to differential equations:

$$g_{\mathbf{g}}(\omega) = -1/G_{\mathbf{g}}(\omega); \quad g_{\mathbf{x}}(\omega) = -1/G_{\mathbf{x}}(\omega),$$
 (B12)

$$\frac{d}{d\omega}g_{g}(\omega) = -1 - \frac{N_{x}\Gamma}{\pi} \frac{1}{g_{x}(\omega)}; \quad g_{g}(-D) = D + \epsilon_{g}, \tag{B13}$$

$$\frac{d}{d\omega}g_{x}(\omega) = -1 - \frac{N_{g}\Gamma}{\pi} \frac{1}{g_{g}(\omega)}; \quad g_{x}(-D) = D + \epsilon_{x}, \tag{B14}$$

$$\frac{d}{d\omega} \left[ a_{g}(\omega) |g_{g}(\omega)|^{2} \right] = -\frac{N_{x} \Gamma}{\pi} a_{x}(\omega), \tag{B15}$$

$$\frac{d}{d\omega} \left[ a_{\mathbf{x}}(\omega) |g_{\mathbf{x}}(\omega)|^2 \right] = -\frac{N_{\mathbf{g}} \Gamma}{\pi} a_{\mathbf{g}}(\omega). \tag{B16}$$

Removing the  $\omega$  dependence, we find the relationship between  $g_{\rm g}$  and  $g_{\rm x}$ , in terms of the integration constant which connects the low energy and high energy states.

$$\frac{g_{\rm g}}{D + \epsilon_{\rm g}} = \exp\left[\frac{\pi(\epsilon_{\rm g} - \epsilon_{\rm x})}{N_{\rm g}\Gamma}\right] \exp\left[-\frac{\pi(g_{\rm g} - g_{\rm x})}{N_{\rm g}\Gamma}\right] \left[\frac{g_{\rm x}}{D + \epsilon_{\rm x}}\right]^{N_{\rm x}/N_{\rm g}}.$$
 (B17)

Since the zero temperature analysis is meaningful only when  $D \gg \epsilon_{g,x}$ , we will replace  $D + \epsilon_{g,x}$  by D. That is,

$$\frac{g_{\rm g}}{T_0} = \exp\left[-\frac{\pi(g_{\rm g} - g_{\rm x})}{N_{\rm g}\Gamma}\right] \left[\frac{g_{\rm x}}{\Delta}\right]^{N_{\rm x}/N_{\rm g}},\tag{B18}$$

$$T_0 = D \left[ \frac{\Delta}{D} \right]^{N_{\rm x}/N_{\rm g}} \exp \left[ \frac{\pi (\epsilon_{\rm g} - \epsilon_{\rm x})}{N_{\rm g} \Gamma} \right],$$
 (B19)

$$\Delta = \frac{\Gamma}{\pi}.\tag{B20}$$

And

$$\frac{d}{d\omega} \left[ N_{g} a_{g}(\omega) g_{g}(\omega) + N_{x} a_{x}(\omega) g_{x}(\omega) \right] = N_{g} a_{g}(\omega) + N_{x} a_{x}(\omega).$$
 (B21)

Due to the sharpness of Fermi function at the Fermi level, the spectral functions have a sharp cut-off at the threshold energy  $E_0$ . Since  $A_n(\omega)$  vanishes below this cut-off energy,  $\Sigma_n(\omega)$  is purely real and  $g_n(\omega)$  does not vanish or cross the frequency axis below the threshold energy  $E_0$ . That is,  $g_n(\omega)$  is positive definite below the threshold energy  $E_0$ .

#### 1. Leading asymptotic behavior

We can derive the asymptotic behavior near the cut-off energy. Since  $a_{\rm g}(\omega)$  and  $g_{\rm x}(\omega)$  vanish at  $\omega = E_0$ , we can approximate the above equations:

$$E_0 - \omega = \int_0^{g_x} dy \frac{g_g(y)}{g_g(y) + N_g \Delta} \approx \frac{1}{N_g \Delta} \int_0^{g_x} dy \ g_g(y), \tag{B22}$$

$$E_0 - \omega = \int_0^{g_g} dy \frac{g_x(y)}{g_x(y) + N_x \Delta} \approx \frac{1}{N_x \Delta} \int_0^{g_g} dy \ g_x(y), \tag{B23}$$

$$\frac{g_{\rm g}}{T_0} \approx \left[\frac{g_{\rm x}}{\Delta}\right]^{N_{\rm x}/N_{\rm g}}$$
 (B24)

Here  $\Delta = \Gamma/\pi$ . From the above, we can find

$$\frac{g_{\rm g}(\omega)}{T_0} \approx |\tilde{\Omega}|^{\alpha_{\rm g}},$$
 (B25)

$$\frac{g_{\rm x}(\omega)}{\Delta} \approx |\tilde{\Omega}|^{\alpha_{\rm x}},$$
 (B26)

$$T_0 = D \left[ \frac{\Delta}{D} \right]^{N_x/N_g} \exp \left[ \frac{\pi(\epsilon_g - \epsilon_x)}{N_g \Gamma} \right], \tag{B27}$$

$$\alpha_{\rm g} = \frac{N_{\rm x}}{N_{\rm g} + N_{\rm x}}; \quad \alpha_{\rm x} = \frac{N_{\rm g}}{N_{\rm g} + N_{\rm x}}, \tag{B28}$$

$$\tilde{\Omega} \equiv (N_{\rm g} + N_{\rm x}) \frac{E_0 - \omega}{T_0}.$$
(B29)

Since the zero temperature analysis is based upon the assumption  $|\epsilon_n| \ll D$ , the realistic Kondo energy scale is given by the replacement of  $D + \epsilon_n \to D$ . The asymptotic behavior right above the cut-off  $E_0$  can be found from the expressions below  $E_0$  by the analytic continuation:

$$\frac{g_{\rm g}(\omega + i\delta)}{T_0} \approx e^{-i\alpha_{\rm g}\pi} \tilde{\Omega}^{\alpha_{\rm g}}, \tag{B30}$$

$$\frac{g_{\mathbf{x}}(\omega + i\delta)}{\Delta} \approx e^{-i\alpha_{\mathbf{x}}\pi} \tilde{\Omega}^{\alpha_{\mathbf{x}}}, \tag{B31}$$

$$A_{\rm g}(\omega) \approx \frac{1}{\pi T_0} \sin(\alpha_{\rm g} \pi) |\tilde{\Omega}|^{-\alpha_{\rm g}} \theta(\omega - E_0),$$
 (B32)

$$A_{\rm x}(\omega) \approx \frac{1}{\pi \Delta} \sin(\alpha_{\rm x} \pi) |\tilde{\Omega}|^{-\alpha_{\rm x}} \theta(\omega - E_0).$$
 (B33)

Here the phase was determined such that the spectral function is positive definite above the threshold energy. Since  $[N_g a_g g_g + N_x a_x g_x]_{\omega=E_0} = 1$ , we can deduce that

$$a_{\rm g}(\omega) \approx \frac{1}{(N_{\rm g} + N_{\rm x})T_0} \tilde{\Omega}^{-\alpha_{\rm g}} \theta(E_0 - \omega),$$
 (B34)

$$a_{\rm x}(\omega) \approx \frac{1}{(N_{\rm g} + N_{\rm x})\Delta} \tilde{\Omega}^{-\alpha_{\rm x}} \theta(E_0 - \omega).$$
 (B35)

From the above asymptotic expressions, we find

$$\rho(\omega) \approx \frac{1}{\Gamma} \frac{1}{(N_{\rm g} + N_{\rm x})^2} B(\alpha_{\rm x}, \alpha_{\rm g}) \begin{cases} \sin(\alpha_{\rm g} \pi) \ \theta(\omega) \\ \sin(\alpha_{\rm x} \pi) \ \theta(-\omega) \end{cases}$$

$$= \frac{1}{\Delta} \frac{1}{[N_{\rm g} + N_{\rm x}]^2}, \tag{B36}$$

$$\chi_{\rm g}''(\omega) \approx \frac{1}{\pi T_0} \frac{\sin(\alpha_{\rm g}\pi)}{(N_{\rm g} + N_{\rm x})^2} B(\alpha_{\rm x}, \alpha_{\rm x}) \operatorname{sgn}(\omega) |\tilde{\omega}|^{1-2\alpha_{\rm g}},$$
 (B37)

$$\tilde{\omega} \equiv (N_{\rm g} + N_{\rm x}) \frac{\omega}{T_0}.$$
 (B38)

Here B(p,q) is the beta function.

## 2. Next leading asymptotic behavior

From the above analysis, we can see that it is more appropriate to use the dimensionless quantities. Here we collect all the relevant formulas from the above.

$$\frac{d}{d\tilde{\Omega}}\frac{g_{\rm g}}{T_0} = \alpha_{\rm g} \left[ \frac{1}{N_{\rm x}} + \frac{\Delta}{g_{\rm x}} \right]; \quad g_{\rm g}(-D) = D + \epsilon_{\rm g}, \tag{B39}$$

$$\frac{d}{d\tilde{\Omega}}\frac{g_{x}}{\Delta} = \alpha_{x} \left[ \frac{T_{0}}{N_{g}\Delta} + \frac{T_{0}}{g_{g}} \right]; \quad g_{x}(-D) = D + \epsilon_{x}, \tag{B40}$$

$$\frac{d}{d\tilde{\Omega}} \left[ a_{g}(\omega) |g_{g}(\omega)|^{2} \right] = \alpha_{g} \Delta T_{0} a_{x}(\omega), \tag{B41}$$

$$\frac{d}{d\tilde{\Omega}} \left[ a_{\mathbf{x}}(\omega) |g_{\mathbf{x}}(\omega)|^2 \right] = \alpha_{\mathbf{x}} \Delta T_0 \ a_{\mathbf{g}}(\omega), \tag{B42}$$

$$E_0 - \omega = \int_0^{g_x} dy \frac{g_g(y)}{g_g(y) + N_g \Delta},$$
(B43)

$$E_0 - \omega = \int_0^{g_g} dy \frac{g_x(y)}{q_x(y) + N_x \Delta},\tag{B44}$$

$$\frac{g_{\rm g}}{T_0} = \exp\left[-\frac{\pi(g_{\rm g} - g_{\rm x})}{N_{\rm g}\Gamma}\right] \quad \left[\frac{g_{\rm x}}{\Delta}\right]^{N_{\rm x}/N_{\rm g}}.$$
 (B45)

Expanding the last relation, we get

$$\frac{g_{\rm g}}{T_0} = \left[\frac{g_{\rm x}}{\Delta}\right]^{N_{\rm x}/N_{\rm g}} \left(1 + \frac{g_{\rm x}}{N_{\rm g}\Delta} - \frac{T_0}{N_{\rm g}\Delta} \left[\frac{g_{\rm x}}{\Delta}\right]^{N_{\rm x}/N_{\rm g}} + \cdots\right). \tag{B46}$$

Then it is straightforward to show that

$$\frac{g_{\rm g}}{T_0} = \tilde{\Omega}^{\alpha_{\rm g}} \left[ 1 - g_1 \, \tilde{\Omega}^{\alpha_{\rm g}} + 2g_2 \, \tilde{\Omega}^{\alpha_{\rm x}} + \cdots \, \right], \tag{B47}$$

$$\frac{g_{\mathbf{x}}}{\Lambda} = \tilde{\Omega}^{\alpha_{\mathbf{x}}} \left[ 1 + 2g_1 \; \tilde{\Omega}^{\alpha_{\mathbf{g}}} - g_2 \; \tilde{\Omega}^{\alpha_{\mathbf{x}}} + \cdots \; \right], \tag{B48}$$

$$g_1 = \frac{1}{N_{\rm g} + 2N_{\rm x}} \frac{T_0}{\Delta}; \quad g_2 = \frac{1}{2N_{\rm g} + N_{\rm x}}.$$
 (B49)

Furthermore, writing in the Taylor expansion form,

$$a_{\mathbf{g}} = \frac{1}{[N_{\mathbf{g}} + N_{\mathbf{x}}] T_0} \tilde{\Omega}^{-\alpha_{\mathbf{g}}} \left[ 1 + a_1 \tilde{\Omega}^{\alpha_{\mathbf{g}}} + a_2 \tilde{\Omega}^{\alpha_{\mathbf{x}}} + \cdots \right] \theta(\tilde{\Omega}), \tag{B50}$$

$$a_{\mathbf{x}} = \frac{1}{[N_{\mathbf{g}} + N_{\mathbf{x}}] \Delta} \tilde{\Omega}^{-\alpha_{\mathbf{x}}} \left[ 1 + b_1 \tilde{\Omega}^{\alpha_{\mathbf{g}}} + b_2 \tilde{\Omega}^{\alpha_{\mathbf{x}}} + \cdots \right] \theta(\tilde{\Omega}).$$
 (B51)

we can find the following relations

$$b_1 = 2a_1 - 4g_1; \quad \alpha_{\rm g}b_2 = a_2 + 4g_2,$$
 (B52)

$$\alpha_{\mathbf{x}}a_1 = b_1 + 4g_1; \quad a_2 = 2b_2 - 4g_2.$$
 (B53)

Finally we find

$$a_{\rm g} = \frac{1}{[N_{\rm g} + N_{\rm x}] T_0} \tilde{\Omega}^{-\alpha_{\rm g}} \left[ 1 + 0 \tilde{\Omega}^{\alpha_{\rm g}} - 4g_2 \tilde{\Omega}^{\alpha_{\rm x}} + \cdots \right] \theta(\tilde{\Omega}), \tag{B54}$$

$$a_{\mathbf{x}} = \frac{1}{[N_{\mathbf{g}} + N_{\mathbf{x}}] \Delta} \tilde{\Omega}^{-\alpha_{\mathbf{x}}} \left[ 1 - 4g_1 \tilde{\Omega}^{\alpha_{\mathbf{g}}} + 0 \tilde{\Omega}^{\alpha_{\mathbf{x}}} + \cdots \right] \theta(\tilde{\Omega}). \tag{B55}$$

And the pseudo spectral functions are

$$A_{g} = \frac{1}{\pi T_{0}} |\tilde{\Omega}|^{-\alpha_{g}} \left[ \sin(\alpha_{g}\pi) - 2g_{2} \sin[(\alpha_{g} - \alpha_{x})\pi] |\tilde{\Omega}|^{\alpha_{x}} + \cdots \right] \theta(-\tilde{\Omega})$$

$$= \frac{\sin(\alpha_{g}\pi)}{\pi T_{0}} |\tilde{\Omega}|^{-\alpha_{g}} \left[ 1 + 4g_{2} \cos(\alpha_{g}\pi) |\tilde{\Omega}|^{\alpha_{x}} + \cdots \right] \theta(-\tilde{\Omega}), \tag{B56}$$

$$A_{\mathbf{x}} = \frac{\sin(\alpha_{\mathbf{g}}\pi)}{\pi\Delta} |\tilde{\Omega}|^{-\alpha_{\mathbf{x}}} \left[ 1 - 4g_1 \cos(\alpha_{\mathbf{g}}\pi) |\tilde{\Omega}|^{\alpha_{\mathbf{g}}} + \cdots \right] \theta(-\tilde{\Omega}).$$
 (B57)

The scaling dimensions found here all agree with those found in the conformal field theory for the overcompensated cases.

### 3. Physical quantities

Using the above results, we can find the dynamic susceptibilities for the ground and the excited configurations

$$\chi_{\rm g}''(\omega) = \operatorname{sgn}(\omega) \frac{\sin(\alpha_{\rm g}\pi)}{(N_{\rm g} + N_{\rm x})^2 \pi T_0} \times \left[ B(\alpha_{\rm x}, \alpha_{\rm x}) \ |\tilde{\omega}|^{1-2\alpha_{\rm g}} - 4g_2 \ [1 - \cos(\alpha_{\rm g}\pi) \ ] \ B(\alpha_{\rm x}, 2\alpha_{\rm x}) \ |\tilde{\omega}|^{2-3\alpha_{\rm g}} + \cdots \right], \quad (B58)$$

$$\chi_{\rm x}''(\omega) = \operatorname{sgn}(\omega) \frac{T_0 \sin(\alpha_{\rm x}\pi)}{(N_{\rm g} + N_{\rm x})^2 \pi \Delta^2} \times \left[ B(\alpha_{\rm g}, \alpha_{\rm g}) \ |\tilde{\omega}|^{1-2\alpha_{\rm x}} - 4g_1 \ [1 - \cos(\alpha_{\rm x}\pi) \ ] \ B(\alpha_{\rm g}, 2\alpha_{\rm g}) \ |\tilde{\omega}|^{2-3\alpha_{\rm x}} + \cdots \right]. \quad (B59)$$

These correlation functions are directly proportional to the imaginary part of the corresponding dynamic correlation functions. The functional forms are marginal Fermi liquid type for the case  $N_{\rm g}=N_{\rm x}$ , which correspond to the overcompensated case. The convoluted atomic electron spectral functions are

$$\rho_{\rm f}(\omega > 0) = \frac{\sin(\alpha_{\rm g}\pi)}{(N_{\rm g} + N_{\rm x})^2 \pi \Delta} \\
\times \left[ B(\alpha_{\rm x}, \alpha_{\rm g}) - 4g_1 \ B(\alpha_{\rm x}, 2\alpha_{\rm g}) \ |\tilde{\omega}|^{\alpha_{\rm g}} + 4g_2 \ \cos(\alpha_{\rm g}\pi) \ B(\alpha_{\rm g}, 2\alpha_{\rm x}) |\tilde{\omega}|^{\alpha_{\rm x}} + \cdots \right], \quad (B60)$$

$$\rho_{\rm f}(\omega < 0) = \frac{\sin(\alpha_{\rm x}\pi)}{(N_{\rm g} + N_{\rm x})^2 \pi \Delta} \\
\times \left[ B(\alpha_{\rm x}, \alpha_{\rm g}) + 4g_1 \ \cos(\alpha_{\rm x}\pi) \ B(\alpha_{\rm x}, 2\alpha_{\rm g}) |\tilde{\omega}|^{\alpha_{\rm g}} - 4g_2 \ B(\alpha_{\rm g}, 2\alpha_{\rm x}) \ |\tilde{\omega}|^{\alpha_{\rm x}} + \cdots \right]. \quad (B61)$$

One important observation is that the scaling dimensions agree with those obtained from the conformal field theory treatments for the overcompensated multichannel S=1/2 models. From this result, we can argue that the convoluted local electron spectral function is peaked right at the Fermi level (Kondo resonance) for the overcompensated models. This result seems to be independent of the occupancy of the ground level. In fact, the numerical results with NCA confirm this conclusion. Hence we conclude that Kondo resonance peak in the overcompensated models sits right at the Fermi level irrespective of any model parameters. In the single channel Anderson model, the position of the Kondo resonance peak is adjusted by the Friedel sum rule (Fermi liquid ground state). That is, the occupancy of the ground configuration determines the Kondo resonance peak position.

We can also generate the low temperature dependence of some physical quantities. Resistivity and thermopower can be evaluated using the Kubo formula.

$$\rho(T) = \rho(0) \left( 1 - c \left[ \frac{T}{T_0} \right]^{\nu} \right); \quad \nu = \min(\alpha_g, \alpha_x), \tag{B62}$$

$$Q(T) \propto \left[\frac{T}{T_0}\right]^{\nu}$$
 (B63)

## APPENDIX C: CONDUCTION ELECTRON SCATTERING RATE.

Here we derive the conduction electron scattering time in the presence of the Anderson magnetic impurities. In general, the conduction electron scattering rate (the inverse of the conduction electron lifetime) is different from the transport scattering rate. This difference derives from the vertex correction when we calculate the current-current response function. The simplifying feature of the Anderson model is that only one partial wave state is coupled to the atomic electron state for an isotropic hybridization. In this simplified model, the transport scattering rate is proportional to the imaginary part of the conduction electron self energy.

The conduction electron scattering time is given by the angular average of the anisotropic one.

$$\tau_{\mu\nu}(\omega) = 3 \int \frac{d\hat{k}}{4\pi} \, \hat{k}_{\mu} \hat{k}_{\nu} \, \tau_{\mu\nu}(\hat{k}, \omega). \tag{C1}$$

Since  $\tau_{\mu\nu}(-\hat{k},\omega) = \tau_{\mu\nu}(\hat{k},\omega)$  in the Anderson model, the scattering time matrix becomes diagonal. Thus we have

$$\tau_{\mu\mu}(\omega) = \int \frac{d\hat{k}}{4\pi} \, \hat{k}_{\mu} \hat{k}_{\mu} \, \tau(\hat{k}, \omega). \tag{C2}$$

In the dilute Anderson impurity limit, the conduction electron self energy can be approximated by [6]

$$\Sigma(\vec{k}\alpha, i\omega) = N_{\text{imp}} \sum_{i} |\langle \vec{k}\alpha | V | i \rangle|^2 G_i(i\omega), \tag{C3}$$

$$\tau^{-1}(\vec{k}\alpha,\omega) = 2\pi N_{\text{imp}} \sum_{i} |\langle \vec{k}\alpha | V | i \rangle|^2 \rho_i(\omega). \tag{C4}$$

Here the index i is the atomic electron's good quantum number. We can write the self energy as

1. With LS coupling, but without CEF.

$$\Sigma(\vec{k}\alpha, i\omega) = N_{\rm imp} \sum_{jm} |\langle \vec{k}\alpha | V | jm \rangle|^2 G_{\rm f}(j; i\omega), \tag{C5}$$

$$G_{\rm f}(j;\tau) = -\langle T_{\tau} f_{jm}(\tau) f_{jm}^{\dagger}(0) \rangle, \tag{C6}$$

$$\langle \vec{k}\alpha|V|jm \rangle = \sum_{m_3\beta} \langle \vec{k}\alpha|V|m_3\beta \rangle \langle 3m_3; \frac{1}{2}\beta|jm \rangle,$$
 (C7)

The total angular momentum is a good quantum number in this case.

2. With both LS coupling and CEF.

$$\Sigma(\vec{k}\alpha, i\omega) = N_{\text{imp}} \sum_{jcd_c} |\langle \vec{k}\alpha | V | \Gamma_c^{(j)} d_c \rangle|^2 G_f(\Gamma_c^{(j)}; i\omega), \tag{C8}$$

$$G_{\rm f}(\Gamma_c^{(j)};\tau) = -\langle T_{\tau} f_{\Gamma_c^{(j)} d_c}(\tau) f_{\Gamma_c^{(j)} d_c}^{\dagger}(0) \rangle,$$
 (C9)

$$\langle \vec{k}\alpha|V|\Gamma_c^{(j)}d_c \rangle = \sum_m \langle \vec{k}\alpha|V|jm \rangle \langle jm|\Gamma_c^{(j)}d_c \rangle.$$
 (C10)

The CEF irreps are good quantum numbers.

In the above, two successive unitary transformations have been used.

$$f_{m_3\alpha} = \sum_{jm} \langle 3m_3; \frac{1}{2}\alpha | jm \rangle f_{jm}$$
 (C11)

$$f_{jm} = \sum_{cd_c} \langle jm | \Gamma_c^{(j)} d_c \rangle f_{\Gamma_c^{(j)} d_c}.$$
 (C12)

For the isotropic, spin-independent hybridization and the free electron conduction band, the mixing matrix is given by

$$<\vec{k}\alpha|V|m_3\beta> = \sqrt{\frac{4\pi}{\Omega}} V(k)Y_{3m_3}(\hat{k}) \delta_{\alpha\beta}$$
 (C13)

$$V(k) = \sqrt{4\pi} \ (-i)^3 \int dr \ r^2 j_3(kr) V(r) R_f(r). \tag{C14}$$

$$<\vec{k}\alpha|V|jm> = \sqrt{\frac{4\pi}{\Omega}} V(k) < \hat{k}\alpha|jm>$$
 (C15)

$$<\hat{k}\alpha|jm> = \sum_{m_3} Y_{3m_3}(\hat{k}) < 3m_3; \frac{1}{2}\alpha|jm>$$
 (C16)

$$<\vec{k}\alpha|V|\Gamma_c^{(j)}d_c> = \sqrt{\frac{4\pi}{\Omega}} V(k) < \hat{k}\alpha|\Gamma_c^{(j)}d_c>$$
 (C17)

$$<\hat{k}\alpha|\Gamma_c^{(j)}d_c> = \sum_{m_3m} Y_{3m_3}(\hat{k}) < 3m_3; \frac{1}{2}\alpha|jm> < jm|\Gamma_c^{(j)}d_c>.$$
 (C18)

Here  $\Omega$  is the volume of the system. Hence the conduction electron self energy in the isotropic hybridization can be written as

$$\Sigma(\vec{k}\alpha, i\omega) = 4\pi n_{\text{imp}} |V(k)|^2 \sum_{jm} |\langle \hat{k}\alpha | jm \rangle|^2 G_f(j; i\omega), \tag{C19}$$

$$= 4\pi n_{\text{imp}} |V(k)|^2 \sum_{jcd_c} |\langle \hat{k}\alpha | \Gamma_c^{(j)} d_c \rangle|^2 G_f(\Gamma_c^{(j)}; i\omega).$$
 (C20)

Here only the diagonal elements of Green's function are nonvanishing.

#### 1. Without CEF

When the CEF is neglected, the conduction electron self energy in a dilute impurity limit reads

$$\Sigma(\vec{k}\alpha, i\omega) = 4\pi n_{\rm imp} |V(k)|^2 \sum_{j} \Theta^{(j)}(\hat{k}) G_f(j; i\omega), \tag{C21}$$

$$\tau^{-1}(\vec{k}\alpha, \omega) = 8\pi^2 n_{\rm imp} |V(k)|^2 \sum_{j} \Theta^{(j)}(\hat{k}) \ \rho_{\rm f}(j; \omega), \tag{C22}$$

$$\Theta^{(j)}(\hat{k}) \equiv \sum_{m} |\langle \hat{k}\alpha | jm \rangle|^2. \tag{C23}$$

 $\rho_{\rm f}(j;\omega)$  is the measurable spectral function for the atomic electrons with the total angular momentum j.

The relevant angular functions defined above are, in fact, constants.

$$\Theta^{(j)}(\hat{k}) = \sum_{m} |\langle \hat{k}\alpha | jm \rangle|^2 = \sum_{\mu d_{\mu}} |\langle \hat{k}\alpha | \Gamma_{\mu}^{(j)} d_{\mu} \rangle|^2 = \frac{2j+1}{8\pi}.$$
 (C24)

#### 2. With CEF

In the presence of the CEF, the CEF irreducible representations are good quantum numbers. The atomic f electron operator can be decomposed into CEF irreducible representation components. Hence the conduction electron self energy in the dilute impurity limit is

$$\Sigma(\vec{k}\alpha, i\omega) = 4\pi n_{\rm imp} |V(k)|^2 \sum_{jc} \Theta_c^{(j)}(\hat{k}) G_f(\Gamma_c^{(j)}; i\omega), \tag{C25}$$

$$\Theta_{\Gamma_c}^{(j)}(\hat{k}) \equiv \sum_{d_c} |\langle \hat{k}\alpha | \Gamma_c^{(j)} d_c \rangle|^2.$$
 (C26)

Here  $\Theta_{\Gamma_c}^{(j)}(\hat{k})$  is crystal harmonics. The anisotropic relaxation rate reads

$$\tau^{-1}(\vec{k}\alpha,\omega) = 8\pi^2 n_{\rm imp} |V(k)|^2 \sum_{jc} \Theta_{\Gamma_c}^{(j)}(\hat{k}) \rho_{\rm f}(\Gamma_c^{(j)};\omega). \tag{C27}$$

Here  $\rho_{\rm f}(\Gamma_c^{(j)};\omega)$  is the measurable spectral function for the atomic f electron of  $\Gamma_c^{(j)}$  symmetry. This spectral function is given by the convolution of two neighboring configuration Green's functions.

In the cubic crystal symmetry, the relevant crystal angular functions are

$$\Theta_7^{(5/2)}(\hat{k}) = \sum_{\alpha} |\langle \hat{k} \uparrow / \downarrow | \Gamma_7^{(5/2)} \alpha \rangle|^2 
= -\frac{1}{32\pi} \left[ 35\cos^4\theta - 30\cos^2\theta - 5 + 5\sin^4\theta\cos 4\varphi \right], \qquad (C28) 
\Theta_8^{(5/2)}(\hat{k}) = \sum_{n\alpha} |\langle \hat{k} \uparrow / \downarrow | \Gamma_8^{(5/2)}; n\alpha \rangle|^2 
= \frac{1}{32\pi} \left[ 35\cos^4\theta - 30\cos^2\theta + 19 + 5\sin^4\theta\cos 4\varphi \right]. \qquad (C29)$$

And

$$\Theta_{6}^{(7/2)}(\hat{k}) = \sum_{\alpha} |\langle \hat{k} \uparrow / \downarrow | \Gamma_{6}^{(7/2)}; \alpha \rangle|^{2} 
= \frac{7}{256\pi} [50\cos^{6}\theta - 30\cos^{4}\theta - 10\cos^{2}\theta + \frac{34}{3} 
-10\sin^{4}\theta(5\cos^{2}\theta - 1)\cos 4\varphi], \qquad (C30)$$

$$\Theta_{7}^{(7/2)}(\hat{k}) = \sum_{\alpha} |\langle \hat{k} \uparrow / \downarrow | \Gamma_{7}^{(7/2)}; \alpha \rangle|^{2} 
= \frac{15}{256\pi}\sin^{2}\theta [-14\cos^{4}\theta + 28\cos^{2}\theta + 2 
-2\sin^{2}\theta(7\cos^{2}\theta + 1)\cos 4\varphi], \qquad (C31)$$

$$\Theta_{8}^{(7/2)}(\hat{k}) = \sum_{n\alpha} |\langle \hat{k} \uparrow / \downarrow | \Gamma_{8}^{(7/2)}; n\alpha \rangle|^{2} 
= \frac{1}{32\pi} [-70\cos^{6}\theta + 105\cos^{4}\theta - 40\cos^{2}\theta + \frac{55}{3} 
+5\sin^{4}\theta(14\cos^{2}\theta - 1)\cos 4\varphi]. \qquad (C32)$$

Note that the above crystal angular functions are normalized and satisfy the correct sum rules.

$$\int d\hat{k} \ \Theta_{6,7}^{(j)}(\hat{k}) = 1; \quad \int d\hat{k} \ \Theta_8^{(j)}(\hat{k}) = 2, \tag{C33}$$

$$\sum_{\mu} \Theta_{\mu}^{(j)}(\hat{k}) = \frac{2j+1}{8\pi}.$$
 (C34)

Furthermore, the crystal harmonics for j=5/2 multiplets can be rewritten as

$$\Theta_7^{(5/2)}(\hat{k}) = \frac{1}{16\pi} \left[ 6 - \Phi(\hat{k}) \right]; \quad \Theta_8^{(5/2)}(\hat{k}) = \frac{1}{16\pi} \left[ 6 + \Phi(\hat{k}) \right], \tag{C35}$$

$$\Phi(\hat{k}) = 15\cos^4\theta - 10\cos^2\theta + 1 + 5\sin^4\theta\cos^22\varphi.$$
 (C36)

## REFERENCES

- [1] J. Kondo, Prog. Theor. Phys. **32**, 37 (1964).
- [2] P. W. Anderson, Phys. Rev. **124**, 41 (1961).
- [3] K. G. Wilson, Rev. Mod. Phys. 47, 773 (1975); H. R. Krishna-murthy, J. W. Wilkins, and K. G. Wilson, Phys. Rev. B 21, 1003 & 1044 (1980).
- [4] N. Andrei, K. Furuya, and J. H. Lowenstein, Rev. Mod. Phys. 55, 331 (1983); A. M. Tsvelick and P. B. Wiegmann, Adv. Phys. 32, 453 (1983).
- [5] H. Keiter and J. C. Kimball, Int. J. Mag. 1, 233 (1971).
- [6] N. E. Bickers, Rev. Mod. Phys. 59, 845 (1987); N. E. Bickers, D. L. Cox, and J. W. Wilkins, Phys. Rev. B 36, 2036 (1987).
- [7] J. E. Hirsch and R. M. Fye, Phys. Rev. Lett. 56, 2521 (1986); R. N. Silver, J. E. Gubernatis, D. S. Sivia, and M. Jarrell, Phys. Rev. Lett. 65, 496 (1990).
- [8] I. Affleck and A. W. W. Ludwig, Phys. Rev. Lett. 67, 161 (1991); A. W. W. Ludwig and I. Affleck, Phys. Rev. Lett. 67, 3160 (1991); I. Affleck and A. W. W. Ludwig, Phys. Rev. B 48, 7297 (1993).
- [9] A. W. W. Ludwig, Physica B **199 & 200**, 406 (1994).
- [10] P. Nozières and A. Blandin, J. Phys. (Paris) 41, 193 (1980).
- [11] N. Andrei and C. Destri, Phys. Rev. Lett. **52**, 364 (1984).
- [12] A. M. Tsvelick and P. B. Wiegmann, Z. Phys. 54, 201 (1984); A. M. Tsvelick, J. Phys.
   C 18, 159 (1985); A. M. Tsvelick and P. B. Wiegmann, J. Stat. Phys. 38, 125 (1985).
- [13] P. D. Sacramento and P. Schlottmann, Phys. Lett. A 142, 245 (1989); P. D. Sacramento and P. Schlottmann, Phys. Rev. B 43, 13294 (1991); P. Schlottmann and P. D. Sacramento, Adv. Phys. 42, 641 (1993).

- [14] D. L. Cox and A. E. Ruckenstein, Phys. Rev. Lett. **71**, 1613 (1993).
- [15] P. Nozières, J. Low. Temp. Phys. 17, 31 (1974).
- [16] Tae-Suk Kim and D. L. Cox, Phys. Rev. Lett. **75**, 1622 (1995).
- [17] B. Andraka, Phys. Rev. B 49, 3589 (1994).
- [18] N. Grewe and F. Steglich, in *Handbook on the Physics and Chemistry of the Rare Eraths*, Vol 14, eds. K. A. Gschneidner Jr. and L. L. Eyring (Elsevier, Amsterdam, 1991), p. 343; see Fig. 26 (S(T)), and Fig. 62  $(\chi(T))$ .
- [19] E. A. Gorymychin and R. Osborne, Phys. Rev. B 47, 14280 (1994), for CeCu<sub>2</sub>Si<sub>2</sub>.
- [20] D. L. Cox, Phys. Rev. Lett. 59, 1240 (1987); D. L. Cox, Physica C 153 155, 1642 (1988); D. L. Cox, J. Magn. Magn. Mater. 76 & 77, 53 (1988).
- [21] A. Zawadowski, Phys. Rev. Lett. 45, 211 (1980); A. Muramatsu and F. Guinea, Phys. Rev. Lett. 57, 2337 (1986).
- [22] C. L. Seaman, M. B. Maple, B. W. Lee, S. Ghamaty, M. S. Torikachvili, J.-S. Kang, L. Z. Liu, J. W. Allen and D. L. Cox, Phys. Rev. Lett. 67, 2882 (1991); B. Andraka and A. M. Tsvelick, Phys. Rev. Lett. 67, 2886 (1991).
- [23] H. Amitsuka, T. Hidano, T. Honma, H. Mitamura, and T. Sakakibara, Physica B 186
   188, 337 (1993).
- [24] B. Andraka and G. R. Stewart, Phys. Rev. B 47, 3208 (1993)
- [25] W. W. Kim, J. S. Kim, B. Andraka, and G. R. Stewart, Phys. Rev. B 47, 12403 (1993).
- [26] D. A. Gajewski, P. Allenspach, C. L. Seaman, and M. B. Maple, to appear in *Physica B* (1994).
- [27] F. G. Aliev, S. Vieira, R. Villar, H. P. van der Meulen, K. Bakker, and A. V. Andreev, Pis'ma Zh. Eksp. Teor. Fiz. 58, 814 (1993) [Sov. Phys. JETP Lett. 58, 762 (1993)]; F.

- G. Aliev, H. El Mfarrej, S. Vieira, and R. Villar, Solid State Commun. 91, 775 (1994).
- [28] H. v. Löhneysen, T. Pietrus, G. Portisch, H. G. Schlager, A. Schröder, M. Sieck, and T. Trappmann, Phys. Rev. Lett. 72, 3262 (1994); B. Bogenberger and H. v. Löhneysen, Phys. Rev. Lett. 74, 1016 (1995).
- [29] M. B. Maple, C. L. Seaman, D. A. Gajewski, Y. Dalichaouch, V. B. Barbetta, M. C. de Andrada, H. A. Mook, H. G. Lukefahr, O. O. Bernal, and D. E. MacLaughlin, J. Low. Temp. Phys. 95, 225 (1994).
- [30] D. C. Ralph and R. Buhrman, Phys. Rev. Lett. 69, 2118 (1992); D. C. Ralph, A. W. W. Ludwig, Jan von Delft, and R. A. Buhrman, Phys. Rev. Lett. 72, 1064 (1994); D. C. Ralph and R. Buhrman, Phys. Rev. B 51, 3554 (1995).
- [31] M. Hettler, J. Kroha, and S. Hershfield, Phys. Rev. Lett. 73, 1967 (1994).
- [32] For Ce<sub>1-x</sub>La<sub>x</sub>Cu<sub>6</sub>, see Y. Onuki and T. Komatsubara, J. Magn. Magn. Mater. 63 &
   64, 281 (1987); For Ce<sub>1-x</sub>La<sub>x</sub>Pb<sub>3</sub>, see C. L. Lin, Phys. Rev. Lett. 58, 1232 (1987).
- [33] H. B. Pang and D. L. Cox, Phys. Rev. B 44, 9454 (1991); I. Affleck, A. W. W. Ludwig,H. B. Pang, and D. L. Cox, Phys. Rev. B 45, 7918 (1992).
- [34] Tae-Suk Kim and D. L. Cox, to be published.
- [35] D. L. Cox, Physica B **186 188**, 312 (1993).
- [36] See, for example, M. Tinkham, Group theory and quantum mechanics (McGraw-Hill, New York).
- [37] J. R. Schrieffer and P. A. Wolff, Phys. Rev. **149**, 491 (1966).
- [38] P. W. Anderson, J. Phys. C: Solid St. Phys. 3, 2436 (1970); J. Solyom and A. Zawadowski, J. Phys. F 4, 2269 (1974).
- [39] N. Grewe, Z. Phys. B **52**, 193 (1982).

- [40] Y. Kuramoto, Z. Phys. B **53**, 37 (1983).
- [41] P. Coleman, Phys. Rev. B **29**, 3035 (1984).
- [42] F. C. Zhang and T. K. Lee, Phys. Rev. B **30**, 1556 (1984).
- [43] Th. Pruschke and N. Grewe, Z. Phys. B 74, 439 (1989); Th. Pruschke, Physica B 163, 553 (1990).
- [44] E. Müller-Hartmann, Z. Phys. B 57, 281 (1984).
- [45] D. Jaccard and J. Sierro, *Valence Instabilities*, eds. by P. Watcher and H. Boppart (North-Holland, Amsterdam, 1982) p. 409.
- [46] D. Jaccard, K. Behnia, and J. Sierro, Phys. Lett. A163, 475 (1992).
- [47] J. F. Herbst and J. W. Wilkins, in *Handbook on the Chemistry and Physics of the Rare Earths*, Vol. 10, eds. K. A. Gschneidner and L. Eyring (Elsevier, Amsterdam, 1987), p.321.

## **FIGURES**

FIG. 1. Comparison of experimental resistivity with our numerical calculation. Our numerical calculation shows a  $T^{1/2}$  behavior at low temperatures. Experimental resistivity (points with  $T_0 = 10$  K, from Ref. [17]) is compared with our numerical results. Three different symbols mean a set of three model parameters ( $\square$  for model set 1;  $\bigcirc$  for model set 2;  $\triangle$  for model set 3). The low temperature deviation suggests a possible crossover to a new fixed point.

FIG. 2. Crystal electric field energy level scheme for  $f^0, f^1, f^2$  configurations. The one-channel & two-channel Anderson model Hamiltonians are developed from these CEF energy states. The one-channel Kondo model derives from the  $f^0$  singlet and the magnetic  $f^1\Gamma_7$  doublet which mix through hybridization with the  $\Gamma_7$  conduction electrons. The two-channel Kondo model derives from the magnetic  $f^1\Gamma_7$  doublet and the nonmagnetic  $f^2\Gamma_3$  doublet which mix through hybridization with the  $\Gamma_8$  conduction electrons.

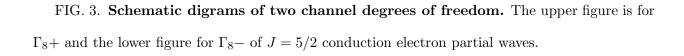


FIG. 4. Scaling diagrams of one-channel & two-channel Anderson model up to third order. Dashed lines are for the  $Ce^{3+}$  impurity  $\Gamma_7$  pseudo spins and the solid lines are for the  $\Gamma_7$  or  $\Gamma_{8n}$  conduction electrons. The diagrams labeled as above lead to the scaling equation for the one-channel exchange coupling,  $J_1$ . To obtain the scaling equations for the two-channel exchange coupling,  $J_2$ , the labels  $\Gamma_7$  for the external conduction electrons (solid lines) should be replaced by  $\Gamma_{8n}$ .

FIG. 5. Leading skeleton self energy diagrams from the NCA. Since two different symmetry conduction electrons are involved in the hybridizations of  $f^0 - f^1$  and  $f^1 - f^2$ , our NCA self energy diagrams become simplified. The diagram (a) is the self energy for the  $f^0$  atomic state (wiggly line). The diagrams (b) are for the  $f^1\Gamma_7$  atomic state (dashed line). The diagram (c) is for the  $f^2\Gamma_3$  atomic state (dotted line). The solid line is the conduction electron propagator: the first two are for the  $\Gamma_7$  and the second two are for the  $\Gamma_8$  conduction electrons.

FIG. 6. Channel dependence of the Entropy. The NCA calculation of entropy clearly shows the right magnitude of residual entropy depending on the relevant channel numbers. Solid lines are Bethe-Ansatz curves. Note that the temperature scale is linear for M=1. Referring to Table I: (a) M=1 case –  $\square$  for model set 8;  $\bigcirc$  for model set 7;  $\triangle$  for model set 6. (b) M=2 case –  $\square$  for model set 1;  $\bigcirc$  for model set 2;  $\triangle$  for model set 3. (c) M=3 case –  $\square$  for model set 4;  $\bigcirc$  for model set 5.

FIG. 7. Channel dependence of the Specific heat. Solid lines are Bethe-Ansatz results. The comparison to the Bethe Ansatz is complicated by the background derived from the inter-configuration peak. In the M=1 cases, the Kondo temperatures are adjusted such that the NCA numerical results fall on the exact Bethe Ansatz one. Thoughout all the figures presented in this paper the estimated Kondo temperatures in the one-channel models are used except for the magnetic susceptibility curves (see Fig. 8). Symbols have the same meaning as in Fig. 6.

FIG. 8. The scaling behavior of the static magnetic susceptibility. The static magnetic susceptibility obeys a scaling behavior for each parameter regime leading to the M=1,2,3 fixed points. The agreement with the Bethe ansatz results (solid lines) is good for the overscreened cases (M=2,3).  $T_0=T_K/0.3$  for M=2,  $T_K$  from Ref. [13]). For convenience, we multiply  $\chi(T)$  by 2.0 for M=2. M=1 case  $-\diamondsuit$  for model set 8;  $\star$  for model set 7;  $\star$  for model set 6; M=2 case  $-\Box$  for model set 1;  $\bigcirc$  for model set 2;  $\triangle$  for model set 3; M=3 case -+ for model set 4;  $\times$  for model set 5. The ground state phase diagram for the model in exchange coupling constant parameter space is drawn in the inset, where  $g_i=N(0)J_i$ , N(0) being the conduction band density of states at the Fermi energy. The solid diagonal line is for M=3.

FIG. 9. Atomic spectral functions in the one-channel regime.  $\rho_{01}$  is the interconfiguration spectral function which is obtained from the convolution between  $f^0$  and  $f^1\Gamma_7$  states.  $\rho_{12}$  is the interconfiguration spectral function which is obtained from the convolution between  $f^1\Gamma_7$  and  $f^2\Gamma_3$  states. One-channel Kondo effect leads to the Kondo resonance development in  $\rho_{01}$  just above the Fermi level and the spectral depletion in  $\rho_{12}$  right at  $\omega = 0$ . Spectral functions are displayed for model set 8. The temperature variations are  $T/D = 3.678 \times 10^{-2}$ ,  $1.077 \times 10^{-2}$ ,  $3.155 \times 10^{-3}$ ,  $9.239 \times 10^{-4}$ ,  $2.706 \times 10^{-4}$ ,  $7.924 \times 10^{-5}$ ,  $2.321 \times 10^{-5}$ .

FIG. 10. Atomic spectral functions in the two-channel regime. Two-channel Kondo effect leads to the Kondo resonance development in  $\rho_{12}$  at the Fermi level (T=0) and the spectral depletion in  $\rho_{01}$  right at  $\omega = 0$ . Spectral functions are displayed for model set 1. The temperature variations are the same as in Fig. 9.

FIG. 11. Atomic spectral functions in the three-channel regime. For this parameter regime (model set 4), two spectral functions are equivalent in the asymptotic limit after a particle-hole transformation. The temperature variations are the same as in Fig. 9.

FIG. 12. Temperature dependence of the Kondo resonance peak. The Kondo resonance peak position  $(\omega_K)$  shows a different temperature dependence on the relevant channel numbers. (a) One-channel case  $(\rho_{01})$ :  $\omega_K$  decreases and saturates to a constant with decreasing temperature. (b) Two-channel case  $(\rho_{12})$  and (c) Three-channel case  $(\rho_{12})$ :  $\omega_K$  decreases and tends to zero with decreasing temperature. Symbols have the same meaning as in Fig. 6. Note the different temperature ranges between M=1 case (top) and M=2,3 cases (bottom).

FIG. 13. Total atomic spectral function. The high energy structure essentially does not depend on either the temperature or the relevant channel numbers. On the other hand, the relevant channel number dependence shows up in the magnitude of the Kondo resonance structure.

(a) One-channel case (model set 8): the Kondo resonance peaks are cut off to be compared with the two- and three-channel cases. (b) Two-channel case (model set 1). (c) Three-channel case (model set 4). The temperature variations are the same as in Fig. 9.

FIG. 14. Variation of  $\chi''(\omega)$  with temperature. The reduced dynamic magnetic susceptibility  $\tilde{\chi}''(\omega,T)/\tilde{\chi}''(\Gamma(T),T)$  is displayed and show a rough scaling behavior between two exrema. One-channel case: model set 8; two-channel case: model set 1; three-channel case: model set 4. The temperature variations are the same as in Fig. 9.

FIG. 15. Peak position ( $\Gamma(T)$ ) of the dynamic magnetic susceptibility. The temperature variation of  $\Gamma(T)$  depends on the relevant channel numbers. In the one-channel case (a),  $\Gamma(T)$  approaches a constant value as  $T \to 0$ . In the two- or three-channel cases (b) and (c),  $\Gamma(T \to 0) \to 0$  which is none other than Marginal Fermi liquid behavior. Symbols have the same meaning as in Fig. 6. Note the different temperature ranges between M=1 case (top) and M=2,3 cases (bottom).

FIG. 16. Angle-averaged scattering rate. (a) One-channel case (model set 8): electron scattering is dominant. The cusp feature for M=1 case right at the Fermi level derives from the spectral depletion of  $\rho_{12}$  and zeros of the crystal harmonic  $\Theta_7^{(5/2)}(\hat{k})$  which is defined in the text. (b) Two-channel case (model set 1): hole scattering is dominant. (c) Three-channel case (model set 4): weak hole scattering dominance over the electron scattering comes from the degeneracy imbalance between the  $f^0$  singlet and  $f^2\Gamma_3$  doublet. The temperature variations are the same as in Fig. 9.

FIG. 17. Low temperature dependence of resistivity. Correct power laws are found asymptotically for the finite temperature NCA calculation in the two- and three-channel cases. A power law of  $T^{1/2}(T^{2/5})$  is expected for M = 2(M = 3). Symbols have the same meaning as in Fig. 6.

FIG. 18. Channel dependence of the thermopower. The thermopower is a measure of asymmetry in the density of states and the scattering rate with respect to the Fermi level. Large thermopower derives from the Kondo resonance scattering. For M = 1, the holes are main carriers leading to positive thermopower. For M = 2,3, electrons are dominant carriers leading to a negative thermopower. The thermopower for M = 2 compares favorably with the experiments for the stoichimetric system,  $CeCu_2Si_2$ . For more details, see the text.

TABLES

Model parameters for the Ce impurity. This set of model parameters covers the single, three, and two channel Kondo regimes.  $\Gamma = \Gamma_{01} = \Gamma_{12}$  is the hybridization strength for both  $f^0 - f^1$  and  $f^1 - f^2$  mixing, respectively. We scan channel number M = 1, 2, 3 according to whether  $\epsilon_2 > 0, < 0, = 0$ . The Kondo scale  $T_0$  is estimated as described in the text.

Set	M	$\Gamma/D$	$\epsilon_1/D$	$\epsilon_2/D$	$k_BT_0/D$
1	2	0.2	-0.4	-0.1	$1.9081 \times 10^{-3}$
2	2	0.2	-0.37	-0.07	$1.5964 \times 10^{-3}$
3	2	0.2	-0.35	-0.05	$1.3492 \times 10^{-3}$
4	3	0.2	-0.3	0.0	$1.5224 \times 10^{-3}$
5	3	0.2	-0.4	0.0	$6.9413 \times 10^{-3}$
6	1	0.2	-0.3	0.05	$1.1957 \times 10^{-3}$
7	1	0.2	-0.3	0.07	$1.6740 \times 10^{-3}$
8	1	0.2	-0.3	0.10	$2.3914 \times 10^{-3}$